PHYSICAL REVIEW D VOLUME 9, NUMBER 5 1 MARCH 1974

Measurement of *p-p* inclusive cross sections at very high energy*

L. G. Ratner
Accelerator Division, Argonne National Laboratory, Argonne, Illinois 60439

R. J. Ellis† and G. Vannini‡
Department of Physics, University of Bologna, 40126 Bologna, Italy

B. A. Babcock,§ A. D. Krisch,‖ and J. B. Roberts
Randall Laboratory of Physics, University of Michigan, Ann Arbor, Michigan 48104

(Received 20 February 1973)

We measured the differential inelastic cross section $Ed^3\sigma/dP^3$ for particles produced in very-high-energy proton-proton collisions at the CERN Intersecting Storage Rings. We studied the inclusive reaction $p+p\rightarrow x+$ anything, where x was a π^+, K^+, or proton. The momenta of the two colliding beams varied from 15.3 to 26.5 GeV/c. This was equivalent to a single beam of 500 to 1500 GeV/c hitting a target. We measured the dependence of $Ed^3\sigma/dP^3$ on the transverse and longitudinal momenta of the outgoing particles, $P_\perp$ and $P_\parallel$. We detected these particles with a spectrometer containing magnets and scintillation and Čerenkov counters. The first two magnets steered particles with the correct $P_\perp$ and $P_\parallel$ down the axis of the spectrometer. The third magnet deflected the particles vertically for momentum analysis. A coincidence of the five scintillation counters indicated an event and the Čerenkov counters tagged it as a pion, kaon, or proton. The luminosity was measured by the Van der Meer method. We found that when $Ed^3\sigma/dP^3$ was plotted against $X=P_\parallel/P_{\max}$, it was energy-independent from 12 to 1500 GeV, especially for π^+ data. This supports a type of scaling suggested by Feynman and Yang *et al.* At small X, the pion cross section has a flat maximum, while the proton cross section decreases slightly. When plotted against $P_\perp{}^2$, the pion and proton cross sections both behave as at lower energies: $\sim\exp(-4.0P_\perp{}^2)$. The pion cross section has a distinct forward peak $\exp(-10P_\perp{}^2)$ which is absent in the proton case. The K^+/π^+ ratio is about 10%, with rather poor statistics.

I. INTRODUCTION

Proton-proton collisions have been carefully studied since the construction of the first particle accelerators with the hope of understanding the structure of the proton and its forces. By measuring the distribution of particles emerging from a proton-proton collision, one can study the size of the proton and the nature of its strong interaction. Protons of a few MeV can only elastically scatter, but elastic experiments have given considerable information about the proton. We can learn more about the proton by studying inelastic scattering, which can occur above 300 MeV. In this hundred-MeV range, only pions can be produced. But at about 2 GeV strange particles are first produced and then at about 6 GeV antiproton-proton pairs appear. This GeV region is called high-energy physics.

At energies near 1000 GeV = 1 TeV, many particles are created in a typical inelastic collision. This region, which we call very-high-energy physics, is especially attractive because the production of a particle is no longer affected by threshold kinematic effects. Since we are interested in the dynamics of the p-p interaction and not in kinematics, we want the production of any one particle to be a small perturbation on the total energy of the system.

The study of elastic scattering has yielded a great deal of interesting data and has placed stringent limitations on theoretical models. However, the inelastic cross section is about 75% of the total p-p cross section; thus a knowledge of inelastic scattering is essential to understand strong interactions. While the differential elastic cross section depends on only one variable, inelastic cross sections are complicated functions of the momentum and scattering angle of each of the final-state particles. Since it was not obvious which cross section and which set of variables was best, obtaining useful theoretical results from inelastic experiments has been difficult.

At high energy the total p-p cross section is probably about 41 mb while the number of final states increases rapidly. Therefore the cross sections for most individual inelastic channels such as $p+p\rightarrow p+n+\pi^+$ may each go to zero in the high-energy limit. The study of single-particle spectra, or inclusive cross sections as they are now called, is important at high energy because they do not go to zero. These inclusive experiments[1-3] study the differential cross section for the reaction

$$p + p \rightarrow x + \text{anything}, \tag{1}$$

where x may be a pion, kaon, or proton. An inclusive cross section is thus the sum of the cross sections for all channels which contain the desired final-state particle regardless of what else is present. The reaction $p + p \rightarrow \pi^+ + \text{anything}$ is composed of individual channels such as

$$\begin{aligned} &p + p \rightarrow p + n + \pi^+ , \\ &p + p \rightarrow p + n + \pi^+ + \pi^0 , \end{aligned} \tag{2}$$

etc. Since the number of contributing channels increases rapidly with energy, inclusive cross sections need not vanish at very high energies.[4,5] These cross sections have the further advantage of depending on only three variables: the incident energy and the outgoing particle's momentum and angle. There has been much recent theoretical interest in inclusive cross sections. However, their importance was first stressed by experimentalists and may come primarily from the ease and reliability of their measurement even at the highest energies. In spite of their humble origin, they may ultimately prove the most reliable source of information about very-high-energy interactions.

The present experiment investigated inclusive reactions over the new energy range available at the CERN Intersecting Storage Rings (ISR). We measured the differential production cross sections for π^+, K^+, and p at 18 different points, with the momentum of the outgoing particles between 1.5 and 8.2 GeV/c and with angles between 80 and 200 mrad.

Particles were detected by a telescope of five scintillation counters in coincidence. Two gas threshold Čerenkov counters tagged each particle as a pion, kaon, or baryon and a vertical bending magnet provided momentum analysis. Two steering magnets let us observe particles produced at different angles without physically moving the spectrometer. The ISR luminosity was measured using the Van der Meer method of separating the two ISR beams vertically.

II. THE ISR

The main problem of all high-energy physics experiments is obtaining the high-energy particles. The difficulty in accelerating protons to GeV energies is well illustrated by the size of present-day accelerators, typically 200 meters in diameter, with hundreds of steering and focusing magnets, and with power requirements of many megawatts. The accelerated particles conventionally strike a stationary target. Unfortunately, only a small fraction of the incident energy is then available for creating new particles, since the majority goes into the kinetic energy of the center of mass. However, if two protons of equal energy E_* collide head-on, all of their energy is available for producing new particles. This head-on collision is equivalent to a single proton of energy (E_{lab}) striking a stationary target, where

$$E_{\text{lab}} = 2\frac{E_*^2}{M_p} - M_p . \tag{3}$$

Thus a 1500-GeV proton colliding with a stationary target is equivalent to two 26.5-GeV protons colliding head-on. Physicists have long been interested in colliding beams because of this enormous gain in energy. Other advantages are a considerably smaller accelerator, lower power requirements, and less radiation shielding. Moreover, conventional detectors can be used since all particles have less than 26.5 GeV/c.

Colliding beams use the intersecting storage rings technique,[6-8] where two particle beams, circulating in opposite directions, are stored in rings and collide essentially head-on at an intersection point. The rings themselves are similar to ordinary accelerators, except that the magnets are operated in a dc mode since the particles are not accelerated. The stability of the magnetic fields and the vacuum in the rings are also more critical since the beam circulates for hours, and fluctuations in the magnetic fields and scattering from gas particles will cause beam loss.

In spite of their advantages, colliding beams do have some serious disadvantages. Only charged, stable particles can be stored for a long time, which probably limits storage rings to electrons and protons and their antiparticles.[9] Another problem is the low interaction rate. The interaction rate occurring when a beam of particles strikes a solid target of uniform density is

$$N_{\text{int}} = (I\rho l/e)\sigma , \tag{4}$$

where I is the current of the beam, ρ is the density of the target, l is the target length, e is the electronic charge, and σ is the interaction cross section. When two beams collide, the event rate is[10]

$$N_{\text{int}} = \frac{I_1 I_2}{ce^2 h_{\text{eff}} \tan(\alpha/2)}\, \sigma \equiv L\sigma , \tag{5}$$

where I_1 and I_2 are the currents of the two beams, α is their crossing angle, c is the velocity of light, and h_{eff} is the effective height of the two intersecting beams. Mathematically, $1/h_{\text{eff}}$ is the convolution of the two beams:

$$\frac{1}{h_{\text{eff}}} = \frac{\int N_1(y) N_2(y)\, dy}{\int N_1(y)\, dy \int N_2(y)\, dy} , \tag{6}$$

where $N_1(y)$ and $N_2(y)$ are the vertical distributions of the two beams. The quantity L in Eq. (5) is called the luminosity and is proportional to the event rate. A single beam of 10^{12} particles hitting a 1 cm.-thick target of density 10^{23} particles/cm^3 gives 10^{35} σ interactions. With two intersecting beams of 10^{12} particles, an h_{eff} of 1 cm, and a crossing angle of 200 mrad, there are about 10^{26} σ interactions per second. Thus colliding beams must have much higher intensities than normal accelerator beams to give similar interaction rates. Storage rings also require an outstanding vacuum so that the interaction rate with the residual gas is much less than the beam-beam interaction rate.

The CERN Intersecting Storage Rings are the first proton-proton storage rings. The construction began in 1966 after a three year study, and the ISR was operating by January 1971. Medium-energy electron storage rings were operated successfully in the 1960's [11,12] so the concept was known to be feasible, but the ISR was the first large-scale attempt with protons.

The CERN ISR contain two slightly distorted rings 1 km in circumference which intersect at eight points.[13] At each intersection point the beams pass through straight sections 16.8 m long and intersect at an angle of 14.8°. The ISR is filled with protons transported underground from the CERN Proton Synchrotron (PS) as shown in Fig. 1. A fast kicker magnet ejects a pulse of about 10^{12} protons from the PS into a transfer line to the ISR. It is injected into the inside of one of the rings and then briefly accelerated until it moves about 10 cm toward the outside of the ISR vacuum chamber. The next PS pulse is similarly injected and accelerated slightly less to a position just inside of the previous pulse. This process is repeated until a broad ribbonlike beam about 5 cm wide and 0.5 cm high is "stacked" horizontally in the ring. After a few hundred pulses (approximately 10 minutes) the first ring is filled. A bending magnet in the transfer tunnel then switches the PS pulses into the second ring until that ring is also filled. The direction of circulation is opposite for the two rings. Beams of up to 10 A have been stacked in each ring. The design intensity is[14] 20 A corresponding to 4×10^{14} circulating protons in each ring and would give a 2% momentum spread across each beam. Beams of 10 A give a luminosity of about 2×10^{30} cm^{-2} s^{-1}. Since the total proton-proton cross section is 4×10^{-26} cm^2 this gives an interaction rate of about 8×10^4 per second.

Lower intensity beams were used during our experiment because at that time the decay rates of the higher intensity beams were still rather high so that "clean" measurements were difficult with high luminosity. We usually ran with currents of about 1 to 5 A in each ring. For these currents the decay rates ranged from 0.1%/h to about 2%/h. One reason for these very low decay rates was the excellent vacuum maintained in the ISR beam pipes of about 10^{-10} Torr. These extremely low pressures reduced beam blow-up due to multiple scattering so that beams were maintained for up to 36 hours without restacking. After 36 hours the vertical size of the beams had increased by about a factor of 2, but the beams were still well within the vacuum chamber which was elliptical, 5.2 cm vertically by 16.0 cm horizontally. The stainless-steel vacuum chambers were first exhausted by turbomolecular pumps, while the system was baked out at about 300°C. Sputter ion and titanium sublimation pumps then maintained the ultrahigh vacuum. Pressures were measured with Bayard-Alpert modulated ionization gauges. The vacuum at our intersection consistently averaged 7×10^{-11} Torr as determined by four ion gauges near the crossing point. This excellent vacuum limited the beam-gas interactions to less than 20% of the total event rate. The percentage of beam-gas events is even smaller at higher currents, because the beam-gas event rate is proportional to the current in one beam, while the beam-beam rate goes as the product of the two beam currents.

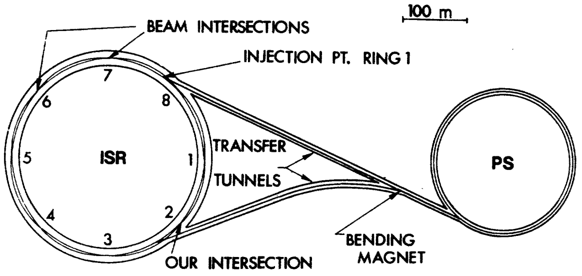

FIG. 1. Diagram of CERN Intersecting Storage Rings (ISR) showing the transfer tunnels for injection from the CERN Proton Synchrotron (PS) and the eight crossing points of the two ISR rings.

The ISR beams were each operated at 15.3, 22.5, and 26.5 GeV/c. These values correspond to single beams of 500, 1100, and 1500 GeV/c striking a stationary target. The momentum spread of the beams was less than 1%, and the angular divergence was about 1 mrad.

III. EXPERIMENTAL APPARATUS

A. Particle detection

Our experiment measured the differential cross section for the production of single particles in the collision of two high-energy protons. The experi-

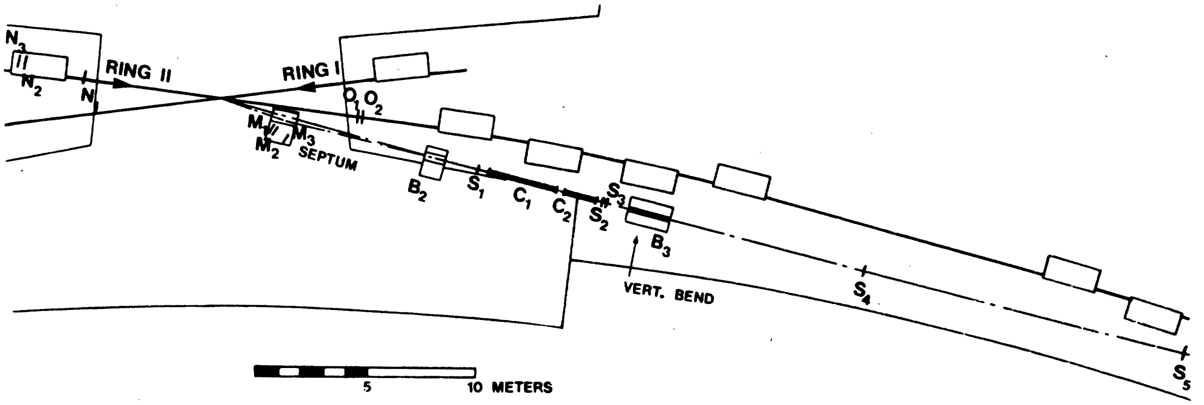

FIG. 2. Layout of the experiment. The two proton beams collide in a diamond-shaped interaction region at the crossing point. The scattered protons and produced mesons are detected by the spectrometer.

mental apparatus, shown in Fig. 2, was a long single-arm spectrometer and three monitor telescopes which all viewed intersection 2 of the ISR. The spectrometer contained three bending magnets to select particles with particular values of momentum and scattering angle, and a telescope of five scintillation counters to signal the passage of a charged particle. Two threshold gas Čerenkov counters, C_1 and C_2, identified each particle as a pion, kaon, or proton. The three magnets allowed us to detect particles with angles between 80 and 200 mrad and momenta between 1.5 and 8.2 GeV/*c* without moving the spectrometer. The three scintillator monitor telescopes *M*, *N*, and *O* measured the luminosity and monitored the beam conditions. Table I is a list of the sizes and positions of the magnets and detectors. Figure 3 shows the positions of the monitors.

The interaction region was a diamond, about 40 cm long × 5 cm wide × 0.5 cm high. The 45-meter length of the spectrometer made the variation of the solid angle subtended for different points within the diamond less than 1%. Thus the event rate did not depend on the particle distribution within

TABLE I. Equipment information.

Scintillation counters	Dimensions (cm) Hor.× Vert.× Length	Distance from the diamond (cm)
S_1	14×8×1.2	1200
S_2	9×10×1.2	1780
S_3	8×9×1.0	1800
S_4	30×18×1.2	3000
S_5	55×20×1.2	4500
M_1 and M_2	46×30×1.2	320 and 350
M_3	41×28×1.2	420
N_1 and N_2	46×30×1.2	640 and 920
N_3	41×28×1.2	940
O_1	33×25×1.2	650
O_2	23×23×1.2	680
Čerenkov counters	Length× i.d. (cm)	Distance to mirror (cm)
C_1	350×17.5	1570
C_2	150×17.5	1730
Magnets	Gap size (cm)	Distance to center (cm)
B_1 (septum)	52×5×120	300
B_2 (*C*)	33×14×100	1000
B_3 (*H*)	14×52×200	2000

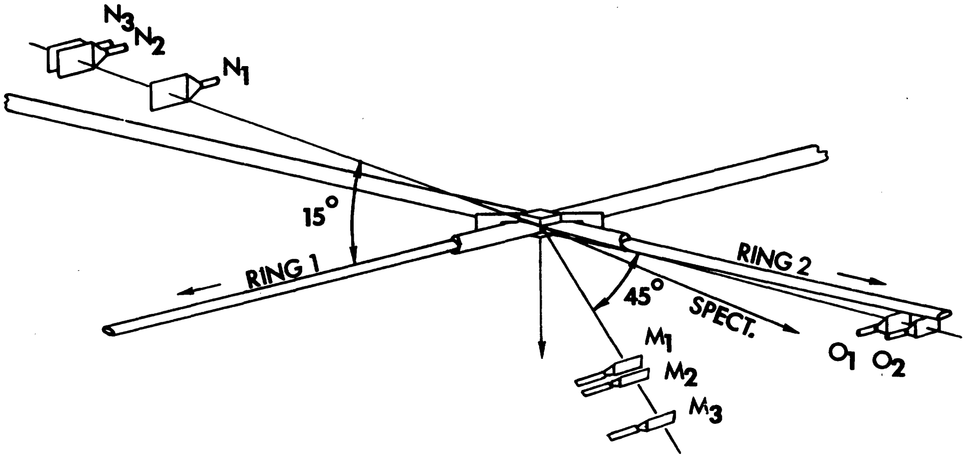

FIG. 3. Layout of the monitor telescopes. Coincidences between the O and N monitors were used to measure the luminosity.

the diamond, which could vary. The long narrow design of the spectrometer also reduced beam-gas and beam-wall background by reducing the length of vacuum chamber viewed by the spectrometer outside the diamond. It also reduced the spread in angle due to the size of the interaction region.

The B_3 magnet bent the particles vertically upward by 100 mrad for momentum analysis. The 20 cm vertical height of S_5 defined the momentum bite of $\pm 4\%$. The momentum smear due to the 0.5 cm height of the interaction region was less than $\pm 0.2\%$. This would have been much greater with horizontal momentum analysis because of the large horizontal size of the interaction region. The S_3 counter defined the angular acceptance both vertically and horizontally, and subtended a solid angle of 2.21×10^{-5} sr. The only purpose of S_1, S_2, and S_4 was to reduce accidentals and they were overmatched.

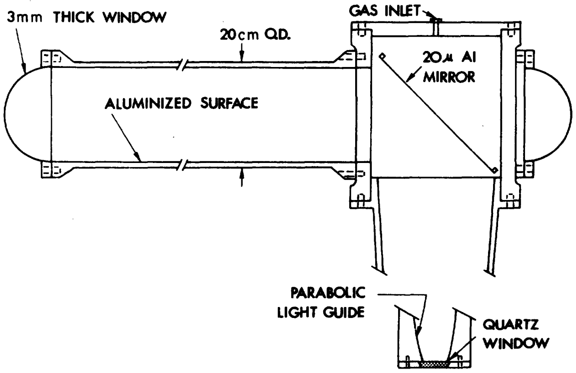

FIG. 4. Diagram of the threshold Čerenkov counters. Particles passed through the horizontal tube from left to right. The mirror reflected their Čerenkov light into the parabolic light funnel and through a quartz window onto a photomultiplier.

All scintillation counters were made of $\frac{1}{2}$-in. thick Pilot B plastic scintillator. All light guides were made of UVT lucite. The light guides were placed alternately to the left and right of the spectrometer axis to eliminate events due to Čerenkov radiation in the lucite. RCA 8575 photomultiplier tubes and ORTEC model 265 bases were used for all the counters. The signals from the photomultipliers were analyzed by Chronetics 100-mHz circuitry. The outputs of the logic network were displayed on 100-mHz TSI scalars. The time-of-flight spectrum of events came from a Chronetics TAC and was accumulated and dispalyed by a TMC 400-channel pulse-height analyzer.

The Čerenkov counters were both standard CERN threshold gas counters[15] as shown in Fig. 4. One was 3.5 m long, the other was 1.5 m, and the inside diameter was 17.5 cm. They had spherical aluminum windows 3 mm thick. A flat mirror at the downstream end of the counter reflected the Čerenkov light produced when a particle passed through the gas into an aluminized parabolic light guide, which focused it onto a 56 DUVP phototube. The counters were filled with either nitrogen or ethylene at pressures of 20 to 500 psia. Both the Čerenkov and scintillation counters were mounted on K and E transit stands capable of translations and rotations both vertically and horizontally.

B. Magnets

The septum magnet was specially designed for this experiment. As shown in Fig. 5 it was 1.2 m long, with a gap of 52 cm wide and 5 cm high. The septum is the thin 4-cm coil at the open side of

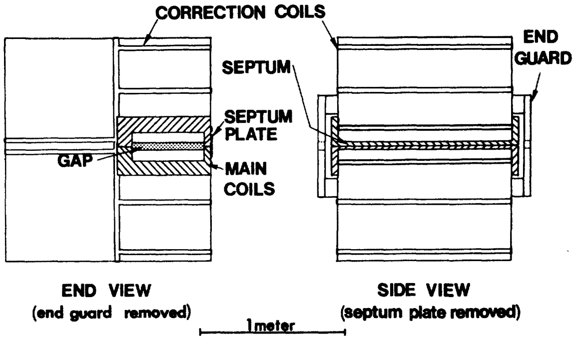

FIG. 5. Diagram of the septum magnet. The thin (5 cm) septum allowed the magnet gap to be close to the ISR vacuum pipe so that particles produced at small angles could be steered into the spectrometer. The correction coils helped cancel any fringe field which might disturb the orbits of the ISR protons.

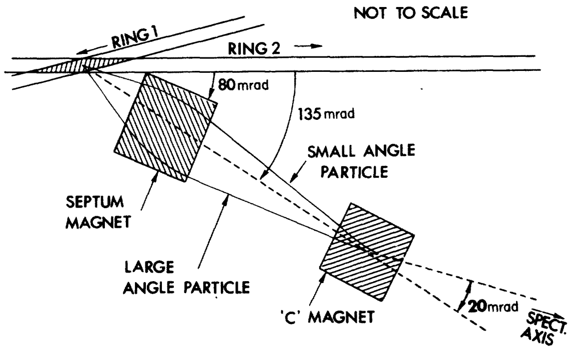

FIG. 6. Steering action of the septum and B_2 magnets. Particles produced at angles less that 135 mrad were bent away from the ISR vacuum pipe by the septum magnet and then realigned along the spectrometer axis by the B_2 magnet. Particles produced at angles larger than 135 mrad were similarly steered.

the gap. This septum allowed the gap to be 5 cm from the ISR vacuum pipe to accept small-angle particles. Because it was close to the ISR beams, we had to reduce the fringe field using special correction coils wrapped around the magnet. Operating the main coils at 591 A and the correction coils at 54.1 A gave an $\int \vec{B}\cdot d\vec{l}$ of 14.46 kGm in the gap. The corresponding fringe field was less than 5 Gm along the ISR beam path, which passed within 6 cm of the septum. Without the correction coils this $\int \vec{B}\cdot d l$ was about 100 Gm. To avoid ISR beam loss we made all current changes very carefully, varying the main and correction coil currents together very slowly.

The other two magnets were standard CERN PS magnets.[16] The B_2 magnet was a one-meter C magnet and B_3 was a two-meter H magnet. Their positions and sizes are listed in Table I. The B_2 magnet was used together with the septum magnet to steer particles produced at angles between 80 and 200 mrad back onto the axis of the spectrometer. This eliminated the problem of rotating the entire spectrometer to view different production angles. For a particle produced at the central angle of 135 mrad, the septum was turned off and the particle went down the central axis of the spectrometer. For a particle at an angle greater than 135 mrad, the septum would bend it toward the ISR and then B_2 realigned it along the central axis. Figure 6 illustrates this steering action. The B_3 magnet provided the 100-mrad vertical bend for momentum analysis.

Each data point was defined by the momentum and production angle of the observed particle. The appropriate field integral for each magnet was then calculated using a kinematics program. The two CERN magnets were calibrated using the CERN PS User's Handbook and checked by nuclear magnetic resonance and rotating coil techniques. The septum magnet was calibrated using $\int \vec{B}\cdot d\vec{l}$ coils and NMR methods at Argonne and then checked at CERN. The calibration of all three magnets was checked periodically using an NMR probe consisting of a Varian F-94 Fluxmeter and a Hewlett Packard 5244L frequency meter. A proton sample was used for fields up to 8 kG, while a deuteron sample was used for higher fields. We believe all magnets were calibrated to an accuracy of $\pm\frac{1}{2}\%$.

C. Phase space

The S_3 counter defined the horizontal and vertical angles accepted by the spectrometer; the solid angle was approximately 2.21×10^{-5} sr. The momentum bit, defined by the 20-cm vertical size of S_5 and the 100-mrad bend of B_3, was about ±4%. A computer program using beam transport matrices[17] calculated the actual particle trajectories. Figure 7 shows the vertical P-ϕ space defined by the S_3 and S_5 counters for a particle coming from the center of the diamond. Only the shaded area is accepted by the spectrometer, since a particle must trigger both S_3 and S_5 to give an event. The S_3 strip is parallel to the P-axis because the vertical bend occurs downstream of S_3. Similar plots for the horizontal P-θ space are shown in Fig. 8. The shaded area shows the range of momentum acceptance, which is defined by the vertical acceptance in Fig. 7. Note that S_3 defines horizontally at all points, since the S_3 strip is well within the S_5 strip over the entire momentum range accepted.

Graphs similar to Fig. 8 were also constructed for particles originating at the extreme edges of

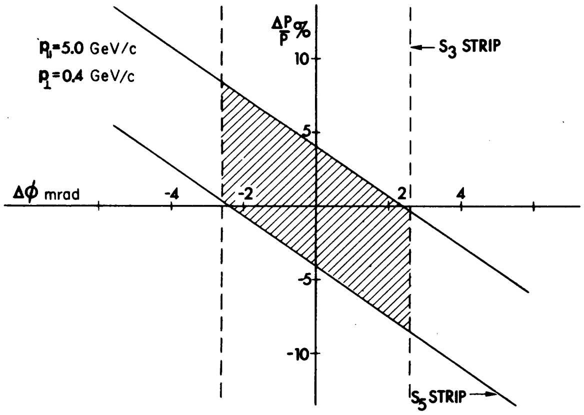

FIG. 7. Plot of the phase space $\Delta\varphi\Delta P/P$ of produced particles. The intersection of the two strips defined by S_3 and S_5 is the phase-space bite subtended by the spectrometer.

the interaction region to be certain that S_3 was always the defining counter. Figure 9 shows the most unfavorable case of a particle emerging from the farthest downstream corner of the diamond. Clearly S_3 is still defining and S_5 is sufficiently overmatched to allow for the large horizontal size of the interaction region.

The total phase-space bite accepted by the spectrometer was the product of the horizontal and vertical acceptances and was typically $\Delta\Omega\Delta P/P = 1.8\times10^{-6}$ sr in the center-of-mass system. The phase space accepted varied slightly with each setting of the spectrometer. The Jacobian for the transformation of this phase-space volume from the c.m. to the laboratory frame was

$$J = \frac{E_{\text{c.m.}} P_{\text{lab}}^2}{E_{\text{lab}} P_{\text{c.m.}}^2} \ . \tag{7}$$

This was typically about 1.03 due to the transverse c.m. velocity of about $0.13c$.

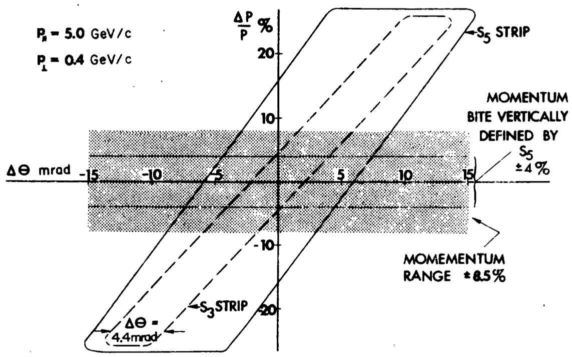

FIG. 8. Plot of the horizontal angle ($\Delta\theta$) accepted by the S_3 and S_5 counters for particles from the center of the interaction region. The momentum range accepted by S_5 is the shaded strip. Thus the horizontal size of S_5 is well overmatched, and so S_3 is defining.

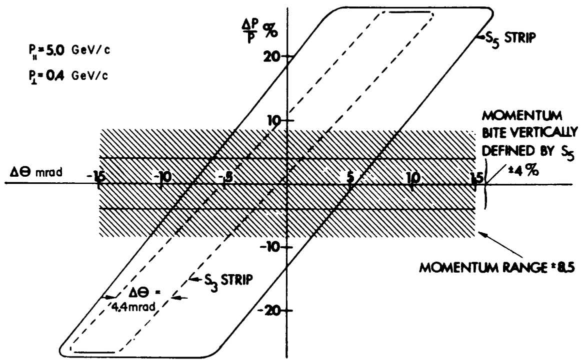

FIG. 9. Plot of the horizontal phase space for particles from the extreme corner of the interaction diamond. Note that S_5 is still overmatched.

D. Monitoring counters

The two monitor telescopes M and N each contained three large scintillation counters. M was located directly below the septum magnet at an angle of about 45° relative to ring 2, as shown in Fig. 3. N was located above ring 2 on the opposite side of the intersection, at an angle of about 15° relative to ring 1. The O monitor contained two scintillation counters and was directly below ring 2 near the spectrometer. Beam-gas and beam-wall collisions produced particles mostly in a sharp cone about the beam direction. Therefore the N monitor viewed mainly ring 1 events, while O and M viewed mainly ring 2 events. To observe beam-beam events we formed the ON and MN coincidences between two monitors viewing different beams. These coincidences should measure the beam-beam event rate, and therefore the luminosity, because when two 25-GeV beam particles collide they generally give two showers going in opposite directions, which will trigger both monitors. However, a single 25-GeV particle colliding with a gas or wall particle generally gives one fast forward shower and perhaps some particles almost at rest; but it rarely gives two fast particles going out in opposite directions. Thus these double-arm coincidence monitors mostly see only beam-beam events. MN was not a very good monitor of beam-beam events because of its geometry. However, ON was a very good monitor since both telescopes were at fairly small angles with respect to the beams, so its beam-gas background was less than

1%. At the same time the two angles were not too small and not equal so that *ON* was not sensitive to elastic and quasielastic events. This made *ON* insensitive to small vertical shifts in the position of the interaction diamond.

An *ON* delay curve is shown in Fig. 10. Accidental coincidences in *ON* produced by beam losses around the rings were monitored with another coincidence, *ON* delay, which was set 50 nsec out of delay. The beam-beam event rate and thus the luminosity was proportional to the difference between *ON* and *ON* delay (ON_d).

IV. EXPERIMENTAL PROCEDURE

Because of the low rates at the ISR, testing the efficiencies and relative timing of the counters were difficult. The counters were tested initially in a beam at the PS and we periodically checked the counters at the ISR.

A. Scintillation-counter tests

High-voltage curves demonstrated that all phototubes were operating properly at the PS. Since it was difficult to obtain good high-voltage curves at the ISR, we placed small light sources on the ends of all the scintillators to check their efficiencies. Each source consisted of a piece of americium foil imbedded in a disk of scintillator.[18] The americium decayed into neptunium plus a 5.5-MeV α particle, which caused the scintillator to emit a light pulse. This source was more dependable than a light diode because the output of a diode changes with age, while the energy of the α particles never changes. The pulse-height distributions produced in each counter by these sources were recorded periodically. A typical pulse-height spectrum is shown in Fig. 11. These spectra were compared with those for previous runs. Any shift in the position of the peak denoted a change in the sensitivity of the phototube, physical damage to the counter, or problems in cable transmission.[19] The rate of each americium source was about 1 kc, and therefore caused no problem with accidentals. However, this rate was fast enough for a high-statistics spectrum to be obtained within a minute. These sources were of no use in the Čerenkov counters because their intensity was too low to produce a detectable signal, so pressure curves were periodically taken at the ISR.

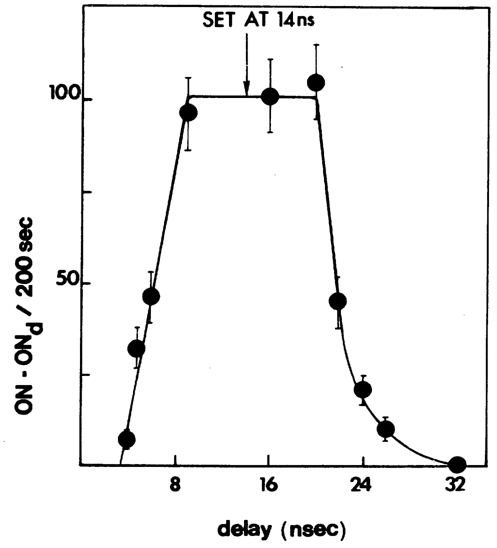

FIG. 10. Timing curve for the coincidence between the *O* and *N* monitors. Lack of counts outside the resolving time showed that this coincidence was not sensitive to beam-gas events, and was a good monitor of beam-beam events and thus the luminosity.

The relative timing of the various scintillation and Čerenkov counters was set by taking delay curves at the PS. We first timed-in the individual coincidences:

$$\begin{aligned} &N = N_1 N_2 N_3\,, \\ &M = M_1 M_2 M_3\,, \\ &O = O_1 O_2\,, \\ &S_{123} = S_1 S_2 S_3\,, \\ &S_{45} = S_4 S_5\,, \\ &C = C_1 C_2 \text{ (or)}. \end{aligned} \tag{8}$$

S_{123} was then timed-in with S_{45} to form S_{fast} with a resolving time of 10 nsec. For detecting pions, S_{fast} was put in coincidence with C_1, which was set just above pion threshold. For detecting kaons, S_{fast} was put in coincidence with C_2 (set just above kaon threshold) and in anticoincidence with C_1 (set below kaon threshold but above pion threshold). Protons were the anticoincidence of C with S_{fast}. A complete diagram of the logic circuitry is shown in Fig. 12. A second coincidence (S_{slow}) was formed between S_{123} and the stretched output of S_{45} to measure the number of accidental triggers in the spectrometer. The ratio of the resolving times of S_{fast} and S_{slow} was 1 : 3; therefore S_{slow} counted three times as many accidentals as S_{fast}. The rate of accidentals in S_{fast} was

$$N_{\text{acc}} = (S_{\text{slow}} - S_{\text{fast}})/2\,. \tag{9}$$

Because the ISR had such a smooth spill, there were essentially no accidentals.

It was not clear in advance that the accidental rates would be insignificant, so we had prepared a second method for checking them. The time of

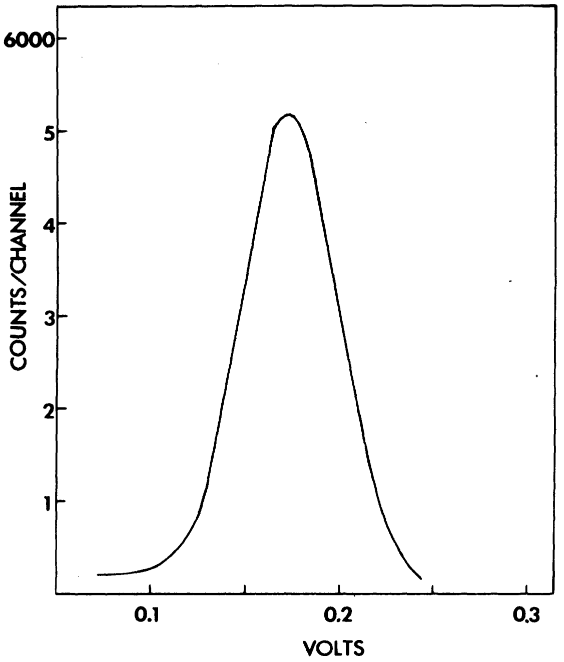

FIG. 11. A sample pulse-height spectrum from the Am^{241} source mounted on S_1. The constant position of the peak showed that the counter was operating properly throughout the experiment.

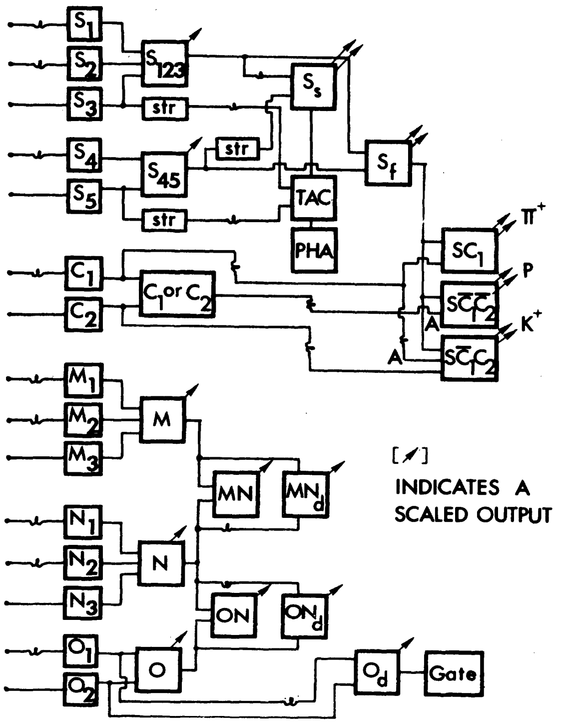

FIG. 12. Schematic of electronic logic for the π, K, and p coincidences, for the monitors, and for the time-of-flight analysis.

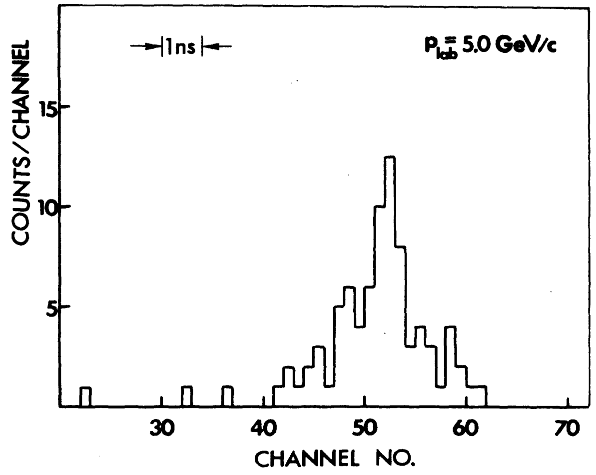

FIG. 13. Time-of-flight spectrum from the pulse-height analyzer. Coincidences are plotted against the time of flight between S_3 and S_5. Lack of events far from the peak shows there are no accidentals.

flight between counters S_3 and S_5 was measured using a time-to-amplitude converter (TAC), which determined the time overlap between stretched pulses from S_3 and S_5 for each S_{slow} coincidence. The TAC output was then accumulated by a pulse-height analyzer (PHA) and displayed at the end of each run. Accidentals appeared as a randomly distributed background, while real events formed a narrow peak. The low accidental rate made this method unnecessary; however, a sample time-of-flight spectrum is shown in Fig. 13.

B. Čerenkov-counter tests

The Čerenkov counters were tuned in a secondary particle beam at the CERN PS. Čerenkov pressure curves indicated that these counters were operating properly and measured their efficiencies. The efficiency of C_1 was measured to be greater than 99.7% and that of C_2 was greater than 99%. We used these pressure curves to construct plots of plateau pressure versus particle momentum. The plot for ethylene is shown in Fig. 14, along with the calculated curves for 0° and 2° for pions, kaons, and protons. Also shown are the curves used to obtain the settings for C_1 and C_2 at each data point. Each counter was operated at a Čerenkov angle slightly greater than 2°. Figure 15 is a typical pressure curve taken at the PS. We also took pressure curves at the ISR to periodically check the counters. One is shown in Fig. 16. These had considerably lower statistics, but showed that there were no gross changes in the threshold settings or the efficiency of the counters.

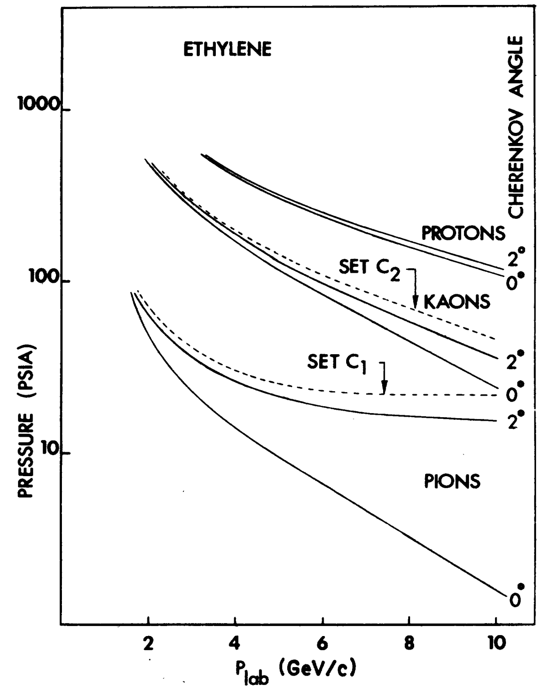

FIG. 14. The 0° and 2° Čerenkov angle curves are shown on a plot of pressure of ethylene against lab momentum for π's, K's, and protons. The dashed lines show the actual settings of the counters.

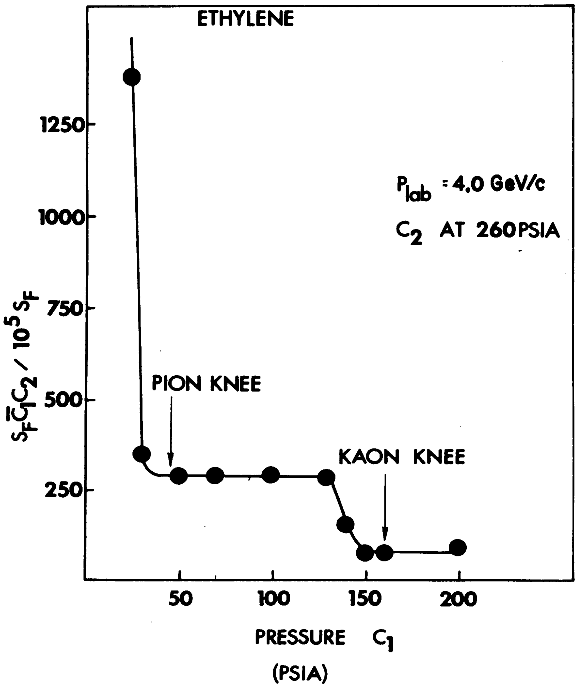

FIG. 15. Anticoincidence Čerenkov pressure curve for C_1 taken at the PS. Note that the rejection efficiency was more tha 99.9%.

C. Beam spikes

Occasionally some of the ISR beam would strike the vacuum chamber wall and produce a large flux of secondary particles. The number of particles in one of these spikes was orders of magnitude larger than the usual number of beam-beam and beam-gas events. These spikes occurred mainly in the magnetic focusing sections of the ISR, where the beam envelope was largest. Because of its long narrow design, our spectrometer viewed only a small region of the beam pipes near the interaction region and was thus fairly insensitive to such spikes. To protect against spikes, we gated all the counters with a coincidence called O_{delay}, which only counted accidentals. As shown in Fig. 12 this was formed by putting the O_1 and O_2 signals far off delay with a 170-nsec resolving time. When a spike occurred the singles rates in both O counters were very high, producing accidental coincidences in O_{delay}. This triggered a 100-μs long gate which blocked all spectrometer and monitor events during that period. Less than 0.1% of real events was lost because of this gate. This gate was tested during stacking in ring 2, when there were many beam-wall interactions. The test involved running the spectrometer with the O_{delay} gate both normally on and off. With the gate normally on we saw only events arriving during a spike. With the gate normally off we vetoed events during

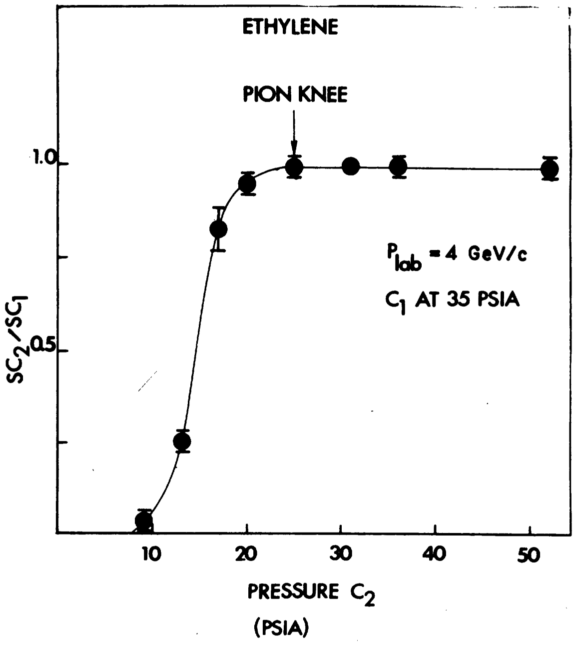

FIG. 16. Čerenkov pressure curve for C_2 taken at the ISR. Despite the poor statistical accuracy, the curve showed that the counter was still operating properly.

spikes. The test showed that we were about 97% efficient in gating out events due to beam-wall spikes. A gate normally on run was also taken during an actual beam-beam run and no events were observed. We concluded that there was no significant contamination due to beam-wall events. This conclusion is also supported by the consistency of the beam-gas background runs which we discuss later.

D. Data recording

The number of pion, kaon, proton, S_{fast}, and S_{slow} coincidences were each counted on two separate scalars to ensure reliability. All other numbers were scaled once ($M, N, O, O_d, MN, ON, MN_d, ON_d, S_{123}$, and S_{45}). The current circulating in each ring was measured by the ISR staff using beam transducers[20] and was displayed on our digital volt meters. A typical run lasted 1000 to 4000 sec depending on the stability of the beams. The time was measured using a one kc signal calibrated with a frequency meter.

The data for each run were recorded by taking a polaroid photograph of all the scalers and printing out the PHA spectrum on paper tape. The current in each ISR ring was recorded several times during each run.

V. LUMINOSITY

A major problem with colliding-beam experiments is measuring a quantity called the luminosity. To appreciate the concept of luminosity, first recall that since Lord Rutherford, all of us have been doing the same scattering experiment. Beams of known intensity but unknown shape have been scattered from a target whose shape or density was very well known and generally uniform. We rarely worry about variations in the interatomic spacing of the atoms in the target. Thus in Lord Rutherford's experiment we have the simple equation

$$\text{Events} = I_0(N_0\rho l)\sigma\,, \tag{10}$$

relating the event rate to the cross section, where I_0 is the total number of incident particles passing through the target, N_0 is Avogadro's number, ρ is the target density in particles/cm^3, and l is the target length in cm.

In a colliding-beam experiment two beams of known intensity, but unknown shapes, collide. Since neither shape is uniform the event rate depends on which portions of the two beams intersect. For example, the event rate will be highest if the maxima of the two intersecting beams coincide, while if the beams miss each other completely, there will be no events. Since the beams cross in the horizontal plane, the event rate is independent of the horizontal shape. To see this consider the fingers of two hands crossing each other in the horizontal plane. Each of the four left fingers crosses each of the four right fingers, independent of whether the fingers are spread apart or squeezed together. However, if we consider the fingers spread in the vertical plane while still crossing in the horizontal plane, then the more they are spread the more they miss each other. Thus for two beams crossing in the horizontal plane, the event rate is fortunately independent of the horizontal shape, but does depend on the vertical shape. This dependence can be parameterized by a quantity called the effective height, h_{eff}.

Quantitatively the event rate in a colliding-beam experiment is given by

$$\text{Events} = L\sigma T\,, \tag{11}$$

where L is the luminosity, σ is the cross section as before, and T is the length of the run in seconds. This luminosity can be written as[10]

$$L = \frac{I_1 I_2}{ce^2 h_{\text{eff}} \tan(\alpha/2)}\,. \tag{12}$$

The currents in the two rings are I_1 and I_2 in A, c and e are the speed of light and the proton charge, while α is the crossing angle of the two beams, 14.8° for the ISR. The effective height as stated previously is

$$\frac{1}{h_{\text{eff}}} = \frac{\int N_1(y)N_2(y)dy}{\int N_1(y)dy \int N_2(y)dy}\,, \tag{13}$$

where $N_1(y)$ and $N_2(y)$ are the functions describing the vertical shapes of the two ISR beams. Thus $1/h_{\text{eff}}$ is the vertical convolution or folding together of the two beams.

The quantities I_1, I_2, T, and α are easy to measure to high precision and e and c are known constants. However, precise measurement of h_{eff} is difficult because it is typically 5 mm or less, so that a ±5% measurement requires a precision of $\pm\frac{1}{4}$ mm. Thus direct measurement by reconstructing all events from an interaction region and then plotting the vertical distribution of the points of origin have so far not succeeded at the necessary precision level.[21]

Instead h_{eff} was measured by a technique suggested by Van der Meer.[22] The ISR staff separated the two beams vertically at the crossing point in a series of small equal steps (1 mm) using vertical steering magnets. Using the ON monitor, which was sensitive only to beam-beam collisions, we observed the number of monitor events as a function of the vertical separation. Such a curve is shown in Fig. 17. Van der Meer showed that the effective height obtained from such a "calibration curve"

$$h_{\text{eff}} = \frac{\sum ON}{ON_{\max}} \tag{14}$$

is identical to the h_{eff} obtained from folding the two beams together as in Eq. (13). Thus the h_{eff} from the calibration curve is the h_{eff} needed to calculate the luminosity in Eq. (12).

In fact, rather than calculating h_{eff} from the calibration curve, the curve can be used to directly calibrate our *ON* monitor. This calibration, once done, is independent of the h_{eff} of the beams used for the calibration curve. This is because the monitor event rate is directly proportional to the luminosity:

$$\text{Events} = ON = L\sigma_{ON}T, \tag{15}$$

where σ_{ON} is the cross section for particles of any type to trigger our *ON* monitor. This σ_{ON} is effectively the calibration constant for our monitor. Recalling the definition of luminosity given in Eq. (12) we get from Eq. (15) that

$$\sigma_{ON} = \frac{ce^2 \tan(\alpha/2) h_{\text{eff}} ON}{I_1 I_2 T} \ . \tag{16}$$

However, $h_{\text{eff}}ON$ is mathematically equal to the area ($\sum ON$) under the calibration curve in Fig. 17. Thus we experimentally determine σ_{ON} from the calibration curve using the equation

$$\sigma_{ON} = \frac{ce^2 \tan(\alpha/2)}{I_1^c I_2^c T^c} \sum_{\text{calb}} ON, \tag{17}$$

where I_1^c, I_2^c, and T^c are the currents and run-duration for each point in the calibration curve. By directly calibrating the monitor we not only make the calibration independent of the ISR beam properties, but we also improve the statistical accuracy of the calibration by using the statistics on the total number of events in the calibration curve. In calculating h_{eff} we are instead limited by the statistics on $ON_{\max}$, the number at the peak of the calibration curve. Of course σ_{ON} does depend on the energy of the ISR beams and we recalibrated for each energy. It also depended on the positions of the monitors, but they did not move.

The major assumption of the Van der Meer method is that the vertical profile of each beam does not change when it is moved vertically away from the ISR median plane. This assumption was tested by an auxiliary experiment using a 10-mm-high beam in ring 1 and a 2-mm beam in ring 2. First the two beams were swept through each other in the normal way, each being simultaneously moved in opposite direction in $\frac{1}{2}$-mm steps. Next the 10-mm beam was held fixed, while the small beam was swept through it in 1-mm steps. Figure 18 shows these two calibration curves, along with the resulting calibration constants which were equal within the statistics of 4%. Using unequal sized beams made this a more critical test of certain types of distortions within the ISR. The results of all our luminosity measurements are shown in Fig. 19. The values of σ_{ON} are plotted at three ISR beam energies. The 5% spread in these points was added in quadrature with the 4% error from the test of the Van der Meer method and the statistical error (~3%) to arrive at an over-all uncertainty of about 7% in σ_{ON}.[23] This error applies in comparing ISR data with accelerator data and in comparing with ISR data at other energies.

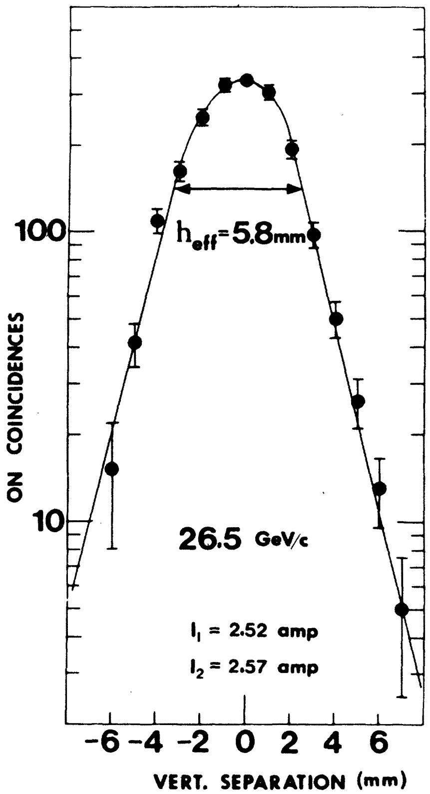

FIG. 17. Plot of *ON* monitor coincidences against the vertical separation of the two beams at intersection 2. This calibration curve was used to obtain the luminosity by the Van der Meer method. The lack of *ON* coincidences at large separation is evidence that we only see beam-beam interactions.

Having measured the calibration constant of the monitor, we can now calculate cross sections from the event rate in the spectrometer and the event rate in the monitor, without worrying about h_{eff}. Combining Eqs. (11) and (15) we have

$$\sigma = \sigma_{ON}\frac{(\text{Events spec})}{(\text{Events } ON)} . \tag{18}$$

VI. BEAM-GAS AND BEAM-WALL BACKGROUND

There are two important backgrounds in colliding-beam experiments. They are beam-gas (BG) and beam-wall (BW) events, while the good events are beam-beam (BB) events. These background events are similar to target-empty events in accelerator experiments. They can be rather serious in colliding-beam experiments because the ISR "target" is itself a beam of very low density (10^8 protons/cm^3) relative to a normal target. The background events come from poor vacuum and the stainless steel walls, whose densities could be similar to those at normal accelerators ($\sim 10^{16}$/cm^3 and $\sim 10^{23}$/cm^3).

Fortunately, the ISR vacuum was outstanding: less than 10^{-10} Torr, mostly of hydrogen. At this vacuum our BG background was about 20% of the BB event rate. If the vacuum had been 10^{-9} Torr the BG background would have been a 200% effect.

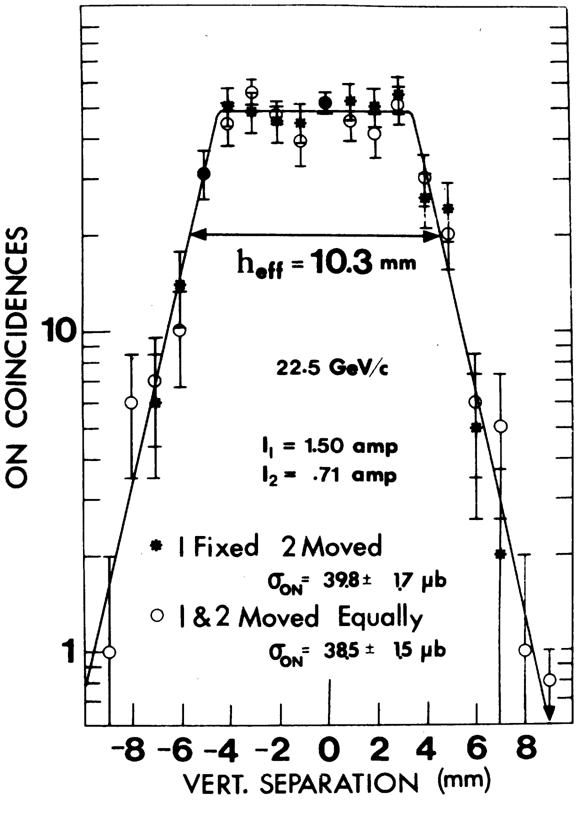

FIG. 18. Test of the Van der Meer method. First both beams are moved simultaneously and then one beam is moved while the other is held fixed. These both gave the same calibration constant within statistical errors.

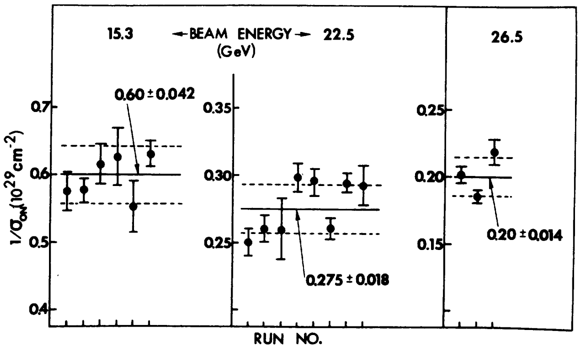

FIG. 19. Plot of the measured values of the calibration constant $1/\sigma_{ON}$. This constant varied with beam energy, but for a fixed energy was constant within the quoted error.

In principle BW background could be more serious than BG background because the stainless-steel vacuum chamber is so dense. In fact most BW events occurred during spikes of μsec length and were gated out of the logic. Most BW interactions occurred more than 15 m from the crossing points so that our spectrometer's sensitivity to these spikes was small.

The beam-gas background was measured by taking runs with beam in only one ring so that BB events were impossible. Since the BG effect was only 20%, such a technique was fairly reliable. However, these runs were not always useful to other groups and we could not take background runs at each data point. The BG correction was interpolated for those data points where there was no background run. To gain confidence in this interpolation, it is useful to consider the beam-gas background theoretically.

First notice that the data runs (a) are the sum of the BB and BG rates, while the background runs (b) were purely BG. Thus we can define a correction factor F:

$$F \equiv \frac{\text{BG}}{\text{BB}} = \frac{b}{a-b} . \tag{19}$$

Next recall that the BB event rate is given by

$$\text{BB} = \frac{I_1 I_2}{ce^2 h_{\text{eff}} \tan(\alpha/2)}\,\sigma . \tag{20}$$

The beam-gas event rate is given by

$$\text{BG} = \frac{I_2}{e}(N_0 \rho l)\sigma_{\text{BG}}, \tag{21}$$

where ρ is the density of gas protons in the vacuum, N_0 is Avogadro's number, and l is the length of vacuum viewed by our spectrometer, which is inversely proportional to the angle of the spectrometer

$$l \approx \frac{A}{\theta}, \tag{22}$$

where A is about 30 cm. The ratio F is then given by

$$F \equiv \frac{\mathrm{BG}}{\mathrm{BB}} = [ceN_0 A \tan(\alpha/2)]\,\rho\left(\frac{h_{\mathrm{eff}}}{I_1\theta}\right)\frac{\sigma_{\mathrm{BG}}}{\sigma_{\mathrm{BB}}}\ . \tag{23}$$

The vacuum pressure was constant to within the accuracy of the gauges so the ρ can be absorbed into the first term which is constant. Fortunately the ratio of the cross sections

$$R_\sigma \equiv \frac{\sigma_{\mathrm{BG}}}{\sigma_{\mathrm{BB}}} \tag{24}$$

is also rather constant as shown in Appendix A. For our largest $P_\perp^2[\sim 1\ (\mathrm{GeV}/c)^2]$, R_σ is as large as 1.2. But for most points this ratio is between 1.00 and 1.05 and can be roughly considered constant.

We now define a ratio F_0 which has the dependence on the spectrometer setting and ISR conditions removed:

$$F_0 = F\frac{I_1\theta}{h_{\mathrm{eff}}} = \frac{\mathrm{BG}}{\mathrm{BB}}\left(\frac{I_1\theta}{h_{\mathrm{eff}}}\right) = \frac{b}{a-b}\left(\frac{I_1\theta}{h_{\mathrm{eff}}}\right)\ . \tag{25}$$

If our analysis of the BG background is correct, this ratio should be constant. In Fig. 20 we show the results of our 20 background runs. F_0 is clearly consistent with being constant. The starred point is from another type of background run taken by spoiling the vacuum by a factor of 100. This should have increased the BG rate by 100, while leaving the BB rate unchanged. The F_0 value was obtained by dividing the observed rate by the measured increase in pressure. In addition F_0 was calculated from Eq. (23) using the measured pressure ρ, the appropriate constants such as c, e, N_0, and R_σ, and the calculated A for our spectrometer acceptance. This calculated point is shown as a diamond. Both these points agree well with the 20 background runs. This not only supports this treatment of BG background, but also suggests that there is little beam-wall background.

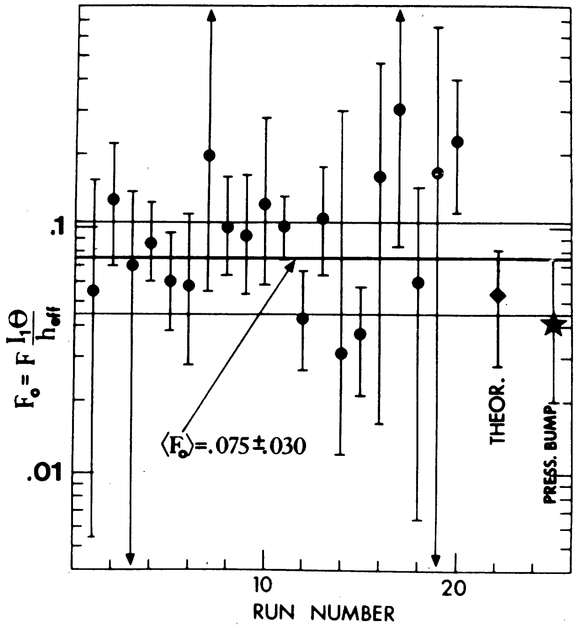

FIG. 20. Plot of the beam-gas correction factor F_0 for all background runs. Its constancy within statistical errors showed that our analysis of beam-gas correction was reliable within the quoted errors. F_0 has units A rad/cm.

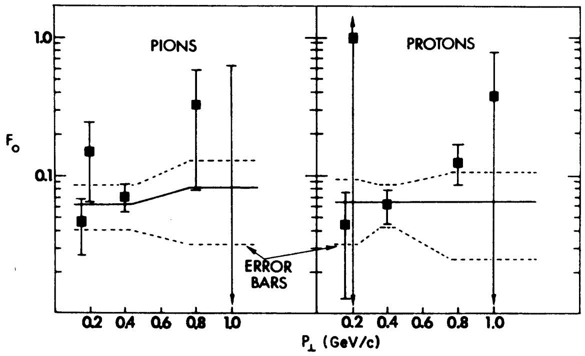

FIG. 21. The measured beam-gas correction factor F_0 plotted against $P_\perp$ for pions and protons. The solid line is our fit to this data described in Appendix A.

Figure 21 is a plot of F_0 versus transverse momentum obtained by averaging the values of F_0 for all different incident energies and longitudinal momentum at each $P_\perp$. The pion and proton data are separated. Figure 22 is a plot of F_0 versus $P_\parallel$ at $P_\perp = 0.4$ GeV/c again summed over all incident energies. As can be seen the statistics are too low to separate both a $P_\perp$ and $P_\parallel$ dependence. We

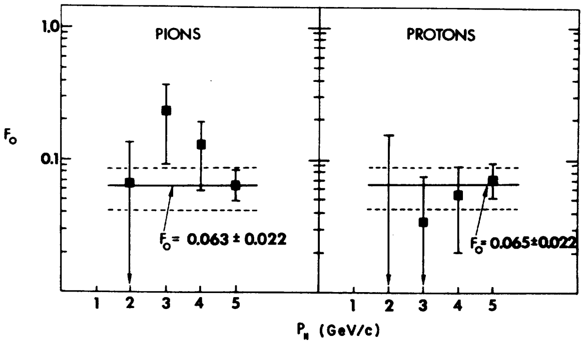

FIG. 22. Plot of F_0 against $P_\parallel$. The solid lines are our fit described in Appendix A.

therefore assumed there is no $P_{\parallel}$ dependence and considered only the $P_{\perp}$ dependence. This is consistent with the theoretical determination of R_{σ} in Appendix A. Moreover, it is clear from Fig. 22 that we are experimentally justified in neglecting the $P_{\parallel}$ dependence to within the quoted errors.

It is partially on the basis of the theoretical determination of R_{σ}(pion) that the solid line fit to the pion data in Fig. 21 has been made. F_0 is taken to be flat for $P_{\perp}$ less than or equal to 0.4 GeV/c, then it gradually increases to about a 25% higher value at 0.8 GeV/c. The errors in F_0 were assigned on the basis of statistics.

The proton cross section is apparently rather flat as a function of X ($\equiv P_{\perp}/P_{\parallel}$). This implies that R_{σ}(proton) is equal to 1, independent of $P_{\perp}$, $P_{\parallel}$, and E_{inc}. This is the basis for the flat fit to the proton data in Fig. 21. The errors are purely statistical.

To make the correction for each data run at a particular transverse momentum we obtained F_0 from Fig. 21 and multiplied it by the appropriate value of $h_{\text{eff}}/I_1\theta$ for that data run. This gave us the value of F. The cross section was then multiplied by the correction factor:

$$C_{BG} = \frac{1}{1+F}\,. \qquad (26)$$

The error in F_0 ranged from 35% to 60% for both pions and protons. Since the actual beam-gas contribution was usually less than 20%, this gave an uncertainty of less than 10% for most data points. The source of this error was mainly statistical, but we treated it as a systematic error in calculating our final cross sections.

VII. CORRECTIONS

Monte Carlo programs were used to calculate the corrections due to decay in flight, multiple Coulomb scattering, nuclear absorption, and positron and muon contamination. Each program traced particles from the interaction region through the entire spectrometer to determine whether or not they were accepted. The programs are described in Appendix B. Each correction factor is the ratio of the number of particles accepted without the effect to the number accepted with the effect included.

A. Decay corrections

A Monte Carlo program computed the corrections to the data for pion and kaon decays in flight. The program assumed that both pions and kaons decayed entirely by the muon-neutrino channel. This introduced a negligible error into the kaon corrections since 85% of kaon decays are two-body decays. The position at which a particle decayed was chosen from a random distribution weighted so that the number of particles decaying at each position fitted the appropriate exponential decay law. Each particle was then traced through the spectrometer up to this point and allowed to decay isotropically in its center-of-mass frame. The decay muon was then transformed into the laboratory frame and traced through the remainder of the system to determine if it was still counted. Off-momentum particles which would not normally have triggered the spectrometer, but whose decay products might, were also considered. Finally, if a kaon decayed in or before C_2, it was considered lost since it would give the wrong Čerenkov signal.

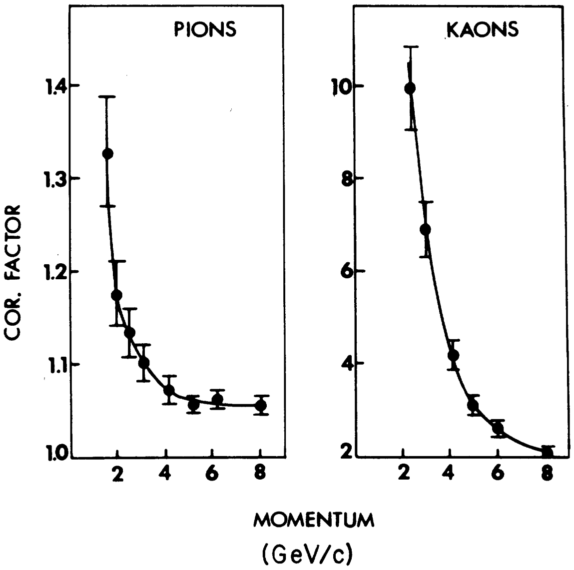

FIG. 23. Decay correction factors for pions and kaons plotted against lab momentum. The points are from the Monte Carlo program. The curve is used for the actual corrections.

As shown in Fig. 23, the correction factors for decay varied from 1.05 to 1.33 for pions. Figure 23 was used for the actual correction factors and the uncertainty was 20% of the correction.

The loss of low-momentum kaons by decay was so great that we only report kaon data for momenta of 4 GeV/c or higher. The kaon correction factor in this range was 3.1 to 4.2, with an uncertainty of only ±10% of the correction since almost all decays were lost.

These computations agree with a simple analytical calculation. The pion correction is consistent with all decays in the first 23 m being lost. This is quite reasonable since the momentum-analyzing magnet, B_3, is located at the 20-m point, and most decays before this magnet should be lost. The kaon correction indicates that all decays in the first 40 m are lost. This is also rather reasonable since the opening angle of the K-decay products is rather large so that very few of the decay products reach the end of the spectrometer.

The decay corrections were insensitive to the particle's position of origin in the diamond. This was because the typical decay angle was larger than the angle subtended by S_5, so that edge effects were not important.

B. Multiple-Coulomb-scattering corrections

We assumed the Coulomb scattering took place at seven different points in the spectrometer, simulating the actual distribution of material. The scattering was Gaussian with a standard deviation equal to the rms scattering angle calculated for the material at each point. We only considered the horizontal scattering because in-scattering was essentially equal to out-scattering in the vertical direction due to the momentum analysis. This gave a continuous flux of particles of varying momenta vertically, and some which would normally miss S_5 were scattered into S_5. Horizontally, S_3 defined the angle and thus there were no particles which normally missed S_5 which could scatter into it.

The correction factor for Coulomb scattering is plotted in Fig. 24 as a function of θ_{rms}, the rms scattering angle for all the material in the spectrometer. The correction factor ranged from 1.00 to 1.16, and was only significant for momenta of 2 GeV/c or less. The uncertainty was ±30% of the correction. Part of this uncertainty came from the dependence on the particle's position of origin in the diamond; particles coming from the extreme corners of the diamond normally passed closer to the ends of S_5 and were more likely to be lost. The correction factor was calculated for central and corner rays and appropriately averaged for a uniform distribution in the diamond. The result was rather insensitive to the averaging.

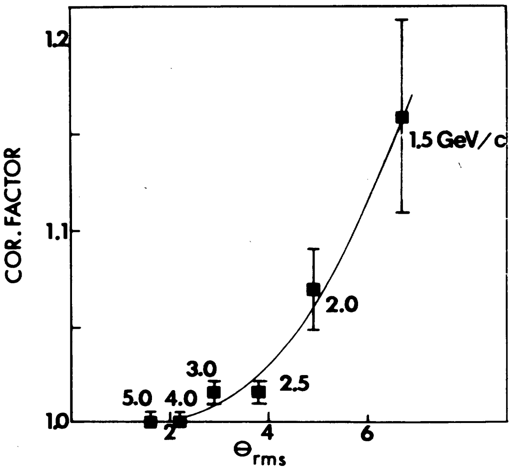

FIG. 24. Multiple scattering correction factors plotted against θ_{rms}, the mean-scattering angle for all the material in the spectrometer. The points are for the Monte Carlo program run at the θ_{rms}, corresponding to the momentum shown. The curve is used for the actual corrections.

There were essentially no particles lost by multiple scattering in the ISR vacuum chamber. In fact the vacuum chamber appeared as a source of particles with a spectrum very similar to the original spectrum because the typical scattering angle of 5 mrad did not significantly change the spectrum. The Monte Carlo program verified that this Coulomb scattering in the vacuum chamber changed the number of particles accepted by less than 1%.

C. Nuclear-absorption corrections

There was also a correction for nuclear interactions of particles in the vacuum chamber and in the spectrometer elements. We used experimental results on total cross sections to calculate the total number of nuclear interactions.[24,25] We then calculated the probability that some particle would still trigger the spectrometer after the original particle interacted. This is described in Appendix B, where for each spectrometer position we calculate the effective rejection efficiency, E, which is is the probability of losing an event if the original particle had a nuclear collision at that position. These calculations include contributions from off-momentum particles which were scattered into the spectrometer by nuclear collisions.

The nuclear absorption correction was obtained from the equation

$$\text{Corr.} = \exp(R_x \sum E L_c) . \qquad (27)$$

L_c is the number of collision lengths of material in each scatterer[24,25] and E is the rejection efficiency for each scatterer. The summation is over all the absorbing material in the spectrometer, which is listed in Table II. The ratio R_x corrects the collision lengths for the difference between the π^+p and K^+p total cross sections and the pp total cross section.[26]

As shown in Table III the nuclear absorption correction factors for pions ranged from 1.16 to 1.41. For protons the range was 1.25 to 1.42, and for kaons 1.13 to 1.14. The uncertainty was estimated to be 20% of the correction, due mainly to

TABLE II. Absorbing material in the spectrometer.

Absorbing element	Collision length of material	Length of element	L_c	E_π	$E_{p,K}$
Air	536 m	15 m	0.028	0.9	0.95
S_0S_1	52.3 cm	2.3 cm	0.044	0.9	0.95
C_1 windows	29.3 cm	0.7 cm	0.024	0.9	0.95
C_1 gas	405 m (CH_2)	$0.238 \times P_{C_1}$(psi) m		0.9	0.95
C_2 windows	29.3 cm	0.7 cm	0.024	0.87	0.95
C_2 gas	405 m (CH_2)	$0.102 \times P_{C_2}$(psi) m		0.87	0.95
S_2S_3	52.3 cm	2.3 cm	0.044	0.87	0.87
S_4	52.3 cm	1.2 cm	0.023	0.7	0.70
Air	536 cm	25 m	0.046	0.7	0.70

the uncertainties in the collision lengths of the various materials in the spectrometer.

Corrections for nuclear interactions in the vacuum chamber were also calculated. A large fraction of the particles could strike the vacuum chamber and scatter into or out of the spectrometer or produce secondaries which might be counted. For particles in the angular range 200 to 80 mrad the vacuum chamber contained 8% to 20% of a collision length, so it scattered, at most, 20% of the particles. Conceivably, more particles could be gained than lost in these nuclear collisions. However, the 5-cm-high gap of the septum magnet restricted the area of the vacuum chamber viewed by the spectrometer so there was a net loss of particles.

As discussed in Appendix B we used a Monte Carlo analysis to determine the correction factors listed in Table IV. For pions the correction factor ranged from 1.02 to 1.17, for kaons the range was 1.08 to 1.10, and for protons, 1.07 to 1.22. The estimated uncertainty was ±30% of the correction, due to uncertainty about the collision length of steel and to the approximations discussed in Appendix B.

TABLE III. Nuclear absorption correction factors for the spectrometer.

$P_\parallel$ (GeV/c)	Correction factors π	K	p
1.5	1.41 ± 8%	···	···
2.0	1.32 ± 6%	···	1.42 ± 8%
2.5	1.29 ± 6%	···	1.37 ± 7%
3.0	1.24 ± 5%	···	1.32 ± 6%
4.0	1.20 ± 4%	1.14 ± 3%	1.29 ± 6%
5.0	1.18 ± 4%	1.13 ± 3%	1.27 ± 5%
6.0	1.17 ± 3%	···	1.26 ± 5%
8.0	1.16 ± 3%	···	1.25 ± 5%

D. Positron correction

Essentially all produced π^0's decayed immediately into two photons. At our spectrometer's small angles, each photon had a 30–60% chance of converting into an electron-positron pair in the vacuum chamber. Since positrons gave the appropriate Čerenkov signals, the pion data included any positrons which reached S_5. Since roughly equal numbers of π^0's and π^+'s were produced, there were about as many positrons as pions entering our $\Delta\Omega\Delta P$ acceptance. Fortunately, most positrons had much lower energy than the pions, since the energy of the initial π^0 was divided four ways. Positrons also lost energy by bremsstrahlung in the vacuum chamber and spectrometer.

TABLE IV. Nuclear absorption correction factors for the vacuum chamber.

$P_\parallel$ (GeV/c)	$P_\perp$ (GeV/c)	Correction factor π	K	p
1.5	0.20	1.10 ± 3%	···	···
2.0	0.16	1.17 ± 5%	···	1.22 ± 7%
2.0	0.20	1.12 ± 4%	···	1.17 ± 5%
2.0	0.25	1.09 ± 3%	···	1.13 ± 4%
2.0	0.30	1.07 ± 2%	···	1.11 ± 3%
2.0	0.35	1.06 ± 2%	···	1.08 ± 3%
2.0	0.40	1.04 ± 1%	···	1.07 ± 2%
2.5	0.20	1.17 ± 5%	···	1.22 ± 7%
3.0	0.40	1.07 ± 2%	···	1.12 ± 4%
4.0	0.40	1.10 ± 3%	1.08 ± 3%	1.16 ± 5%
4.0	0.60	1.06 ± 2%	···	1.11 ± 3%
4.0	0.80	1.03 ± 1%	···	1.07 ± 2%
5.0	0.40	1.13 ± 4%	1.10 ± 3%	1.21 ± 7%
5.0	0.60	1.08 ± 3%	···	1.12 ± 4%
5.0	0.80	1.04 ± 1%	···	1.08 ± 3%
5.0	1.00	1.02 ± 1%	···	1.07 ± 2%
6.0	0.80	1.05 ± 2%	···	1.10 ± 3%
8.0	0.80	1.07 ± 2%	···	1.15 ± 5%

Because of this lower energy, positron contamination was significant only for low-momentum data points. The Monte Carlo program described in Appendix C was used to calculate the appropriate correction.

The correction factors given in Table V are significant only for momenta less than 3 GeV/c. They range from 0.62 to 0.99, with an estimated uncertainty of ±30% of the correction. The uncertainty came mostly from the uncertainty in the initial π^0 and π^+ spectra. The correction varied with incident beam energy because there were more high-momentum π^0's at higher incident beam energy.

During our experiment, we took special runs at the 2-GeV/c, 80-mrad, and 100-mrad points, with different pressures in the Čerenkov counters. These runs tested the positron correction since the average energy loss depended on the amount of gas in the Čerenkov counters. After making only the corrections for nuclear absorption and multiple scattering, the cross sections at different Čerenkov pressures still disagreed. When the appropriate positron corrections were also made, the agreement was significantly better as shown in Table VI. Note that the variations are within the quoted errors.

VIII. CALCULATION OF THE CROSS SECTION AND ERROR

The differential cross section in the c.m. frame was calculated using the equation

$$\left.\frac{d^2\sigma}{d\Omega dP}\right|_{\text{c.m.}} = \frac{\text{Events/sec}}{L\Delta\Omega\Delta P}\,, \tag{28}$$

where L is the luminosity and $\Delta\Omega\Delta P$ is the c.m. phase-space volume accepted by the spectrometer. The relativistically invariant cross section is

$$E\frac{d^3\sigma}{dP^3} = \left(\frac{E}{P^2}\right)\frac{d^2\sigma}{d\Omega dP}\,, \tag{29}$$

where E and P are the energy and momentum of the produced particle.

TABLE V. Positron correction factors.

$P_\parallel$ (GeV/c)	$P_\perp$ (GeV/c)	Incident beam energy (GeV) 15.3	22.5	26.5
1.5	0.20	0.70 ± 9%	0.66 ± 10%	0.62 ± 11%
2.0	0.16	0.78 ± 7%	···	0.65 ± 10%
2.0	0.20	0.82 ± 5%	0.76 ± 8%	0.70 ± 9%
2.0	0.25	···	···	0.78 ± 7%
2.0	0.30	0.87 ± 4%	···	0.87 ± 4%
2.0	0.35	···	···	0.92 ± 3%
2.0	0.40	0.94 ± 2%	0.93 ± 2%	0.91 ± 3%
2.5	0.20	0.86 ± 4%	0.82 ± 5%	0.77 ± 7%
3.0	0.40	0.96 ± 1%	···	···
4.0	0.40	0.98 ± 1%	0.98 ± 1%	0.97 ± 1%
5.0	0.40	0.99 ± 1%	0.98 ± 1%	0.96 ± 1%

The values for the cross sections listed below were obtained by applying the corrections described above to the cross section given above to obtain

$$E\frac{d^3\sigma}{dP^3} = \frac{E}{P^2}\,\frac{\sigma_{ON}}{\Delta\Omega\Delta P}\,\frac{\sum \text{Events}\,ABCDG}{\sum ON}\,. \tag{30}$$

The terms on the right-hand side of Eq. (30) are

E = particle energy,
P = particle momentum.
Events = number of spectrometer counts,
σ_{ON} = luminosity calibration constant,
ON = number of beam-beam monitor events,
$\Delta\Omega\Delta P$ = center-of-mass phase-space volume,
A = beam-gas background correction factor,
B = decay correction factor (for pions and kaons),
C = multiple-Coulomb-scattering correction factor,
D = nuclear-absorption correction factor,
G = positron correction factor (for pions).

Each summation is over all runs at each data point. The sum in the numerator is the corrected number of events for each point, while the sum in the denominator is the total number of monitor counts at that point. Note that the corrections were applied to individual runs, although normally only the beam-gas corrections changed between runs.

TABLE VI. Test of positron corrections.

$P_\parallel$ (GeV/c)	$P_\perp$ (GeV/c)	Pressure	$E(d^3\sigma/dP^3)$, uncorrected [a] mb/(GeV^2/c^3)	$E(d^3\sigma/dP^3)$, corrected [a] mb/(GeV^2/c^3)
2.0	0.20	high	34.6 ± 11%	30.0 ± 11%
2.0	0.20	normal	39.8 ± 13%	30.2 ± 13%
2.0	0.20	low	51.8 ± 11%	36.6 ± 11%
2.0	0.16	normal	49.3 ± 13%	32.1 ± 13%
2.0	0.16	low	73.5 ± 20%	42.2 ± 20%

[a] Errors quoted include only statistical, beam-gas, and luminosity errors.

The total error at each data point was obtained by adding the statistical error in quadrature with the systematic errors in each factor in Eq. (30). The systematic errors for decay, multiple scattering, nuclear absorption, and positrons were usually the same for all runs at each data point. The systematic error for beam-gas background was obtained for each run and the data point error was the appropriately weighted average of these. The total point-to-point error was generally about 15%, and was usually dominated by the statistical error (5–15%), the beam-gas error (4–10%), and the luminosity error (7%). The combined error due to decay, nuclear absorption, multiple scattering, and positron contamination was 4–15%.

In spite of our extensive discussion of errors, an important test of any result is reproducibility. Figure 25 is a plot of the cross section obtained from individual runs at several data points. The consistency under widely varying conditions is evidence of our understanding of various factors contributing to the cross section; in particular, the luminosity measurement and the beam-gas background corrections. Of course the final test must be a remeasurement of these cross section using a completely different spectrometer.[27]

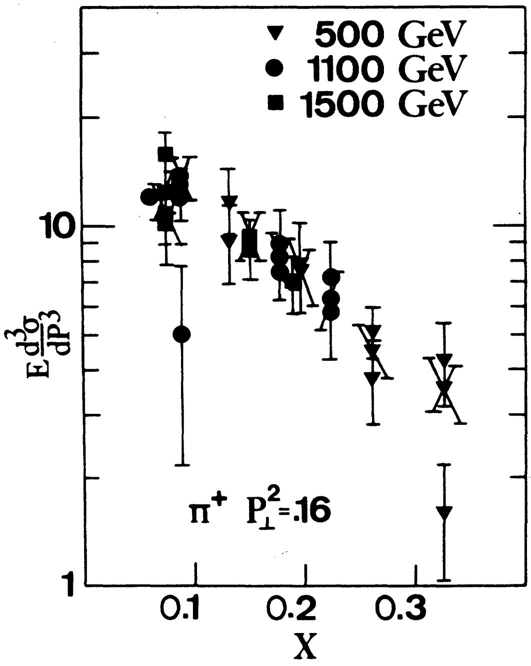

FIG. 25. Plot of $Ed^3\sigma/dP^3$ for separate runs against $X=P_\parallel/P_{\max}$ for several data points. The consistency of different runs at the same data point is evidence for the reliability of our background and luminosity measurements which varied between runs.

IX. RESULTS

This experiment measured the invariant inclusive cross section $E\,d^3\sigma/dP^3$ for π^+, K^+, and protons produced with center-of-mass longitudinal momenta of 1.5 to 8.0 GeV/c and transverse momenta of 0.16 to 1.0 GeV/c. Measurements were made at three ISR beam energies: 15.3, 22.5, and 26.5 GeV. These energies correspond to laboratory beams of 500, 1100, and 1500 GeV striking stationary targets.

The data are tabulated in Table VII. Figures 26 and 27 are plots of most of these data against X and $P_\perp^2$. For comparison, data from accelerator experiments in the 12- to 24-GeV range[1,2] are also shown in Fig. 26.[28] Note that a few of the small X pion points differ by as much as 20% from our preliminary results,[29] due mainly to the positron corrections. Nevertheless, all the pion and proton points still lie within the preliminary error bars. The kaon cross sections are about 50% or 1.2 standard deviations above the preliminary values due to increased decay corrections.

We see from Fig. 26 that when plotted against X, the pion and proton cross sections appear to be independent of incident energy from 12 to 1500 GeV to precisions of about 10% and 20%. The pion cross section apparently has a flat maximum at small X, with no apparent tendency to turn over or peak sharply. The proton cross section decreases slightly at small X.

Due to the poor statistics we can say little about the shape of the kaon cross section. We can only state that the K^+ to π^+ ratio is about 10% in the X range studied.

Looking at $E\,d^3\sigma/dP^3$ plotted against $P_\perp^2$ in Fig. 27, we see that the pion cross section drops as $\exp(-4.0P_\perp^2)$ for $P_\perp^2>0.1$ (GeV/c)^2. The proton cross section is similar, going as $\exp(-3.5P_\perp^2)$. For smaller $P_\perp^2$, the pion cross section has a distinct forward peak of roughly the form $\exp(-10P_\perp^2)$. This peak has been previously observed at accelerator energies as $\exp(-15P_\perp^2)$.[1] There is no evidence for such a peak in the proton cross section. For $P_\perp^2>0.1$ (GeV/c)^2 the X dependence of the pion cross section can be fitted by $e^{-6.7X^2}$, while the proton cross section is better fitted by something like $e^{-3.5(1-X)^2}$. Our experiment gives little information about the X dependence of the pion cross section in the forward peak region [$P_\perp^2<0.1$ (GeV/c)^2]. Thus the cross section for $p+p\rightarrow\pi^+$ +anything can be written as

$$E\frac{d^3\sigma}{dP^3}=Ae^{-(4P_\perp^2+6.7X^2)}+Bf(X)e^{-10P_\perp^2}, \qquad (31)$$

where $f(X)$ is equal to 1 for $X\approx0.1$. The proton inclusive cross section ($p+p\rightarrow p$ +anything) can be

TABLE VII. Final cross sections.

ISR energy:		15.3 GeV		22.5 GeV		26.5 GeV	
$P_\parallel$ (GeV/c)	$P_\perp$ (GeV/c)	X	$E(d^3\sigma/dP^3)$ mb/(GeV$^2/c^3$)	X	$E(d^3\sigma/dP^3)$ mb/(GeV$^2/c^3$)	X	$E(d^3\sigma/dP^3)$ mb/(GeV$^2/c^3$)
Reaction: $p+p\rightarrow\pi^+$ +anything							
1.5	0.20	0.098	30.8 ±21%	0.067	35.9 ±22%	0.057	34.9 ±20%
2.0	0.16	0.131	27.2 ±20%			0.057	32.1 ±19%
2.0	0.20	0.131	22.4 ±17%	0.089	31.6 ±15%	0.075	38.0 ±18%
2.0	0.25					0.075	31.5 ±18%
2.0	0.30	0.131	14.7 ±20%			0.075	22.9 ±17%
2.0	0.35					0.075	19.4 ±18%
2.0	0.40	0.131	10.9 ±19%	0.089	12.8 ±14%	0.075	12.5 ±15%
2.5	0.20	0.163	20.5 ±16%	0.111	26.1 ±17%	0.094	31.6 ±19%
3.0	0.40	0.196	7.6 ±17%				
4.0	0.40	0.261	4.8 ±15%	0.178	8.4 ±15%	0.151	9.9 ±14%
4.0	0.60	0.261	1.4 ±36%	0.178	2.9 ±24%		
4.0	0.80	0.261	0.81 ±55%			0.151	0.92 ±21%
4.3	0.80	0.279	1.0 ±32%				
4.4	0.82			0.195	1.17 ±19%		
5.0	0.40	0.327	3.7 ±16%	0.222	6.6 ±18%	0.189	7.4 ±18%
5.0	0.60			0.222	3.2 ±18%	0.189	3.6 ±20%
5.0	0.80			0.222	0.89 ±19%	0.189	0.81 ±22%
5.0	1.00			0.222	0.29 ±20%		
6.0	0.80	0.392	0.41 ±29%	0.267	0.87 ±18%		
8.0	0.80	0.523	0.11 ±36%	0.356	0.43 ±20%		
Reaction: $p+p\rightarrow K^+$ +anything							
4.0	0.40	0.261	0.74 ±58%	0.178	1.03 ±58%	0.151	0.77 ±66%
5.0	0.40	0.327	0.60 ±44%	0.222	1.44 ±44%	0.189	0.69 ±72%
Reaction: $p+p\rightarrow p$ +anything							
2.0	0.14	0.131	6.0 ±38%			0.075	4.1 ±29%
2.0	0.17	0.131	4.6 ±31%	0.089	4.3 ±20%	0.075	4.0 ±34%
2.0	0.22					0.075	3.2 ±43%
2.0	0.27	0.131	4.8 ±33%			0.075	2.9 ±40%
2.0	0.33					0.075	3.1 ±40%
2.0	0.37	0.131	3.5 ±31%	0.089	3.0 ±22%	0.075	3.7 ±21%
2.5	0.18	0.163	4.9 ±24%	0.111	6.2 ±27%	0.094	5.6 ±30%
3.0	0.38	0.196	5.2 ±20%				
4.0	0.39	0.261	5.3 ±16%	0.178	3.9 ±18%	0.151	3.5 ±18%
4.0	0.59	0.261	1.7 ±35%	0.178	2.1 ±29%		
4.0	0.79	0.261	0.69 ±29%			0.151	0.55 ±27%
4.4	0.79			0.195	0.68 ±23%		
5.0	0.39	0.327	6.1 ±17%	0.222	4.1 ±21%	0.189	4.3 ±22%
5.0	0.59			0.222	3.1 ±19%	0.189	2.7 ±24%
5.0	0.79			0.222	1.1 ±18%	0.189	0.73 ±22%
5.0	0.99			0.222	0.29 ±20%		
6.0	0.79	0.392	1.62 ±19%	0.267	1.03 ±17%		
8.0	0.79	0.523	1.66 ±20%	0.356	1.00 ±17%		

written as

$$E\frac{d^3\sigma}{dP^3}=Ce^{-3.5[P_\perp{}^2+(1-X)^2]}\,. \qquad (32)$$

X. DISCUSSION

Our main result is that when the invariant cross section $E\,d^3\sigma/dP^3$ is plotted against X it appears to be independent of incident energy from 12 to 1500 GeV for the processes

$$\begin{aligned}&p+p\rightarrow\pi^+ + \text{anything},\\&p+p\rightarrow p+\text{anything}.\end{aligned} \qquad (33)$$

The precision of this statement is 10–15% for the π^+ case and perhaps 20% for the proton case. This agrees with a form of scaling proposed by Feynman[4] and Yang *et al.*[5] They predicted that,

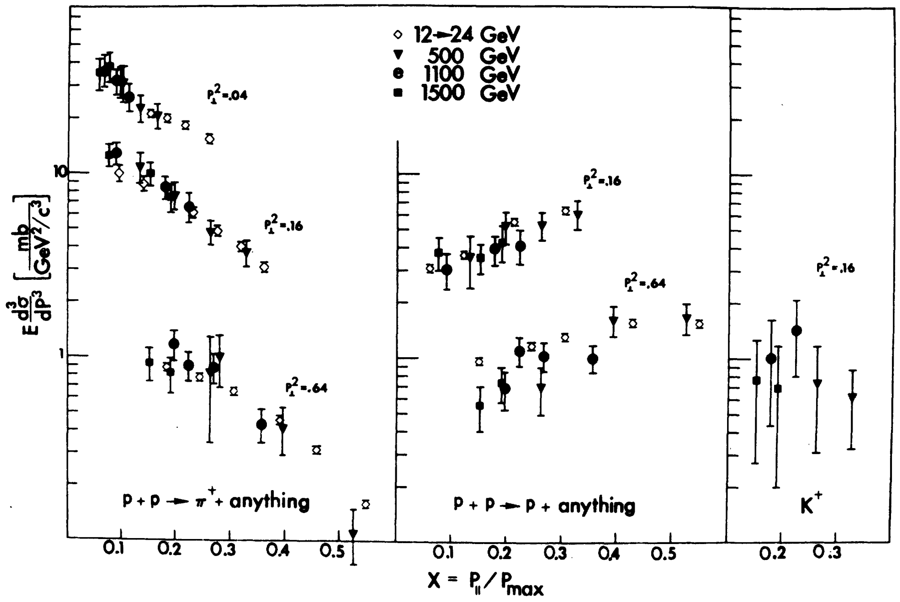

FIG. 26. Plot of the inclusive cross section $Ed^3\sigma/dP^3$ for production of π^+ and K^+ and for proton inelastic scattering as a function of X at fixed $P_\perp^2$. Data are plotted at three ISR energies corresponding to lab beams of 500, 1100, and 1500 GeV, along with accelerator data at 12 and 24 GeV.[1,2]

in the limit of very high energies, the inclusive cross sections for

$$A+B\rightarrow C+\text{anything} \tag{34}$$

would approach a limit. In particular, Feynman suggested that the invariant cross section $Ed^3\sigma/dP^3$ would approach this limit in the center-of-mass system when plotted against the variables X and $P_\perp$. Yang *et al.* proposed that all inclusive cross sections would approach a limiting distribution at very high energies when considered in the rest frame of either the target or the projectile particle. These two statements are equivalent in our kinematic region, so we cannot distinguish between a pionization or one-center model for pion production, and a fragmentation or two-center or fireball or diffraction dissociation model on the basis of our data. Nevertheless, a maximum in the pion cross section at $X=0$ is rather natural in a pionization model, while it seems a little strained in the fragmentation model. The proton cross section does decrease at small X, which supports a fragmentation model. However, this may simply come from the fact that it is difficult for a proton to lose all its energy and emerge at rest. In any case we have chosen to plot the data in the way suggested by Feynman because of its simple invariant form.

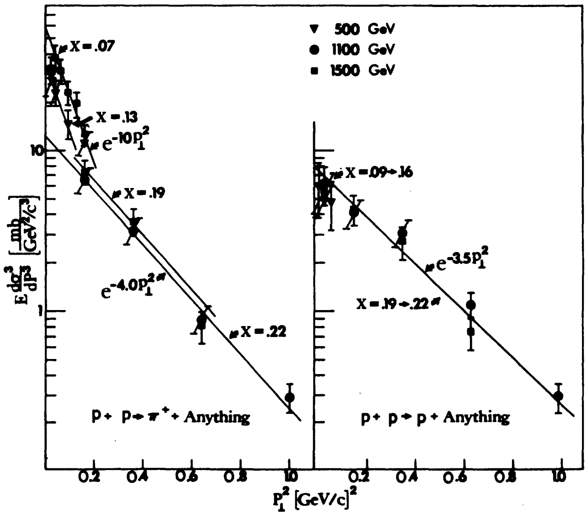

FIG. 27. Plot of $Ed^3\sigma/dP^3$ for pions and protons as a function of $P_\perp^2$, with X held fixed. The straight lines are hand-drawn through the data.

The transverse momentum distributions are also very similar to those at accelerator energies.[1,2] For $P_\perp^2 > 0.1$ (GeV/c)^2, the pion cross section falls off approximately as $\exp(-4P_\perp^2)$. For smaller $P_\perp^2$, the pion cross section has a distinct forward peak of the form $\exp(-10P_\perp^2)$. Yen and Berger[30] have given a natural explanation of this peak. They pointed out that pions from the decays of low-mass "fireballs" or nucleon isobars can pile up at low $P_\perp$. Because of the low Q value of such decays, the pion has approximately the same velocity as the parent N^*. Therefore

$$\langle P_\perp^\pi \rangle \approx \frac{M_\pi}{M_{N^*}} \langle P_\perp^{N^*} \rangle \approx 0.1 \langle P_\perp^{N^*} \rangle . \tag{35}$$

This $P_\perp$ sharpening gives a pion peak. The conspicuous absence of such a peak in the proton $P_\perp$ distribution, which falls off as $\exp(-3.5 P_\perp^2)$ from $0.025 \leqslant P_\perp^2 \leqslant 1.0$ $(\mathrm{GeV}/c)^2$, also supports this explanation. Since $M_p \sim M_{N^*}$, protons should have about the same $P_\perp$ as the parent N^*'s and thus no peak.

One can extend[31] this argument to the longitudinal momentum distribution. The average X of a pion from an N^* decay is

$$\langle X_\pi \rangle \approx \frac{M_\pi}{M_{N^*}} \langle X_{N^*} \rangle \approx 0.1 \langle X_{N^*} \rangle . \tag{36}$$

Since $\langle X_{N^*} \rangle$ is perhaps 0.6, the average X value of pions from these decays is about $\langle X_\pi \rangle \sim 0.06$. Of course there is smearing due to the finite Q values of these resonance decays, but the peaking should still be there. Thus fragmentation may have a sharper X dependence than pionization:

$$\begin{aligned} \left(E\frac{d^3\sigma}{dP^3}\right)_{\mathrm{frag}} &\sim e^{-10X^2} , \\ \left(E\frac{d^3\sigma}{dP^3}\right)_{\mathrm{pion}} &\sim e^{-4X^2} . \end{aligned} \tag{37}$$

The fragmentation model of Yang *et al.*[5] and the field-theoretic model of Feynman[4] both predicted, in advance, the scaling or s independence that we observed. The two models appear somewhat different and finding experimental support for both seems at first somewhat confusing. However, we feel that the s-independent behavior basically arises from the geometrical nature of the proton-proton interaction and that both models are somewhat geometrical in nature. In fact the Lorentz-contracted geometrical model proposed somewhat earlier by Krisch[31] and Huang[32] leads to X being the appropriate variable in inclusive reactions. However, we stress that neither Krisch nor Huang predicted that $E\,d^3\sigma/dP^3$ would be the s-independent form of the cross section.

The geometric nature of Feynman's model can be seen in the assumption that the fields radiated in the interaction are increasingly Lorentz-contracted in the incident direction as s increases. The energy in the fields is a function of $\gamma R_\parallel$ and thus is a function of the canonically conjugate variable

$$X \approx \frac{P_\parallel}{\gamma} . \tag{38}$$

When $Ed^3\sigma/dP^3$ is plotted against X, it should be s-independent by analogy to quantum electrodynamics. The fragmentation model of Yang *et al.* is also somewhat geometric in that it assumes that each incident particle is Lorentz-contracted and fragments into a cloud of particles in its own Lorentz frame, free from the influence of the other cloud.

The Lorentz-contracted geometrical model[31] explains the scaling behavior of the inclusive cross sections and also gives their X and $P_\perp$ dependences. Assuming a Gaussian spherically symmetric interaction region, the inclusive proton and pion cross sections can be obtained by taking Fourier transforms:

$$\begin{aligned} \left(E\frac{d^3\sigma}{dP^3}\right)_{\mathrm{proton}} &= Ae^{-4[P_\perp^2+(1-X)^2]} , \\ \left(E\frac{d^3\sigma}{dP^3}\right)_{\mathrm{pion}} &= Ce^{-4(P_\perp^2+X^2)} . \end{aligned} \tag{39}$$

The proton cross sections from Figs. 26 and 27 are consistent with this form, but the pion cross section exhibits a forward peak in $P_\perp^2$ and a steeper X dependence $[\sim \exp(-6.7X^2)]$. However, as mentioned before, perhaps a fragmentation contribution should be added to this "geometrical pionization" contribution to obtain

$$\left(E\frac{d^3\sigma}{dP^3}\right)_{\mathrm{pion}} = Ae^{-4(P_\perp^2+X^2)} + Be^{-10(P_\perp^2+X^2)} . \tag{40}$$

At fixed $P_\perp^2$, this gives an X dependence more consistent with our data.

Our other interesting result is that the measured K^+/π^+ ratio of about 10% is not much larger than at accelerator energies.[1,2] This suggests that the small cross section for kaon production at accelerator energies is not a threshold kinematic effect and it may never be comparable to pion production. Thus there may be some special reason why strong interactions prefer to produce pions more than kaons.

ACKNOWLEDGMENT

We are especially grateful to Dr. K. Johnson and the ISR staff, for they contributed the most important part of the experiment, the ISR. We thank Dr. G. Giacomelli, Dr. S. W. Gray, and Dr. C. Maroni for their help in various stages of the experiment.

APPENDIX A: THEORETICAL DETERMINATION OF R_σ

We assume the cross section $Ed^3\sigma/dP^3$ is independent of incident energy in our calculation of R_σ, the ratio of beam-beam to beam-gas cross sections. Our final results show that scaling is true to 15%, and since the beam-gas background is about 20%, deviations from scaling should give errors of less than 3%. $Ed^3\sigma/dP^3$ can be written as

$$E\frac{d^3\sigma}{dP^3}=\frac{E}{P^2}\frac{d^2\sigma}{d\Omega dP}\,. \qquad \text{(A1)}$$

Since this cross section is relativistically invariant, it follows that

$$\left(\frac{d^2\sigma}{d\Omega dP}\right)_{\text{lab}}=\left(\frac{E_{\text{c.m.}}P_{\text{lab}}{}^2}{P_{\text{c.m.}}{}^2E_{\text{lab}}}\,\frac{d^2\sigma}{d\Omega dP}\right)_{\text{c.m.}} \qquad \text{(A2)}$$

Then R_σ, which is the ratio of the laboratory beam-gas and beam-beam cross sections, is given by

$$R_\sigma\equiv\frac{(d^2\sigma/d\Omega dP)^{\text{BG}}_{\text{lab}}}{(d^2\sigma/d\Omega dP)^{\text{BB}}_{\text{lab}}}$$

$$=\frac{(E_{\text{c.m.}}P_{\text{lab}}{}^2)^{\text{BG}}/(P_{\text{c.m.}}{}^2E_{\text{lab}})^{\text{BG}}}{(E_{\text{c.m.}}P_{\text{lab}}{}^2)^{\text{BB}}/(P_{\text{c.m.}}{}^2E_{\text{lab}})^{\text{BB}}}\,\frac{(d^2\sigma/d\Omega dP)^{\text{BG}}_{\text{c.m.}}}{(d^2\sigma/d\Omega dP)^{\text{BB}}_{\text{c.m.}}}\,. \qquad \text{(A3)}$$

Since P_{lab} and E_{lab} are each identical for beam-beam and beam-gas events, R_σ becomes

$$R_\sigma=\frac{[(E/P^2)(d^2\sigma/d\Omega dP)]^{\text{BG}}_{\text{c.m.}}}{[(E/P^2)(d^2\sigma/d\Omega dP)]^{\text{BB}}_{\text{c.m.}}}$$

$$=\frac{[(Ed^3\sigma/dP^3)(X,P_\perp)]^{\text{BG}}}{[(Ed^3\sigma/dP^3)(X,P_\perp)]^{\text{BB}}}\,. \qquad \text{(A4)}$$

Recall that $Ed^3\sigma/dP^3$ is apparently independent of incident energy for fixed X and $P_\perp$. For pions in our range of X, $Ed^3\sigma/dP^3$ can be approximated by $f(P_\perp)\exp(-6.7X^2)$, and $f(P_\perp)$ is clearly identical for beam-beam and beam-gas events. Then R_σ reduces to

$$R_\sigma=\exp[6.7X_{\text{BB}}{}^2(1-r^2)]\,, \qquad \text{(A5)}$$

where r is the ratio of the beam-gas and beam-beam X values, which is approximately given by

$$r\equiv\frac{X_{\text{BG}}}{X_{\text{BB}}}=\frac{E_{\text{inc}}}{M}\,\frac{(\cos\theta-\beta_{\text{BG}}/\beta)}{\cos(\theta+\alpha/2)}\,. \qquad \text{(A6)}$$

E_{inc} is the beam energy, M is the proton mass, θ is the laboratory scattering angle, α is the beam intersection angle, β_{BG} is the β of the beam-gas center of mass, and β is the β of the observed particle in the lab.

Using Eq. (A6) we found that R_σ(pion) varied from 1.01 to 1.34. Table VIII lists the values of r and R_σ for pions for the different values of $P_\perp$, $P_\parallel$, and E_{inc} at which background runs were taken. Notice that for a fixed $P_\perp$, R_σ is rather independent of $P_\parallel$. This appears to be verified experimentally in Fig. 22.

TABLE VIII. Calculated values of R_σ for pions.

$P_\perp$ (GeV/c)	$P_\parallel$ (GeV/c)	E_{inc} (GeV)	r	R_σ
0.16	2.00	15.3	0.904	1.02
0.16	2.00	26.5	0.847	1.01
0.20	1.50	26.5	0.651	1.01
0.20	2.50	26.5	0.872	1.01
0.40	2.00	15.3	0.668	1.07
0.40	3.00	15.3	0.847	1.07
0.40	4.00	15.3	0.909	1.09
0.40	5.00	15.3	0.936	1.09
0.40	5.00	22.5	0.917	1.05
0.40	2.00	26.5	0.416	1.03
0.80	4.27	15.3	0.736	1.27
0.80	8.00	15.3	0.916	1.34
0.82	4.39	22.5	0.606	1.17
1.00	5.00	22.5	0.555	1.26

APPENDIX B: CALCULATIONS OF NUCLEAR CORRECTIONS

The initial pion spectrum produced in the interaction region was chosen to fit an invariant cross section of the form

$$E\frac{d^3\sigma}{dP^3}=Ae^{-6.7X^2-6P_\perp}\,, \qquad \text{(B1)}$$

where A was a normalization constant. This spectrum was used in the calculation of all corrections. Our data were better fitted by the formula

$$E\frac{d^3\sigma}{dP^3}=e^{-6.7X^2}(A'e^{-10P_\perp{}^2}+B'e^{-4P_\perp{}^2})\,. \qquad \text{(B2)}$$

However, expression (B1) allowed some useful simplifications in the Monte Carlo routine, and over the range of interest the two expressions were in adequate agreement.

To determine the probability of producing a pion in a given $\Delta\Omega\Delta P$ we converted the invariant cross section into the cross section $d^2\sigma/d\Omega dP$:

$$\frac{d^2\sigma}{d\Omega dP}=\frac{P^2}{E}Ae^{-6.7X^2}e^{-6P_\perp}\,. \qquad \text{(B3)}$$

This expression was further simplified since P^2/E was essentially equal to P. Also since $P_\perp$ was always much smaller than $P_\parallel$, we approximated $P_\parallel$ by P. Thus X became P/P_{max}, where P_{max} was the maximum possible pion momentum. We then obtained a cross section of the form

$$\frac{d^2\sigma}{d\Omega dP}=APe^{-6.7P^2/P_{\text{max}}{}^2}e^{-6P_\perp}\,. \qquad \text{(B4)}$$

We calculated the nuclear absorption corrections for pions, assuming the pions had this initial spectrum. The rejection efficiency for kaons and protons was easily estimated by comparison with the pion efficiencies. We assumed all the material in the spectrometer was bunched at the positions of S_1, S_3, and S_4. Pions generated according to Eq. (B4) were traced through the spectrometer and allowed to have nuclear collisions at these three positions. The resulting collision products were traced through the remainder of the system to determine if they were accepted.

For each collision we assumed that 25% of the events were elastic.[25] We assumed the remaining inelastic events contributed the scattered primary plus 1.5 secondaries. We chose 1.5 because the charge multiplicity is about 1 - 2 (Ref. 33) at energies of 2 to 8 GeV. The elastic scattering angle was taken from the formula $\exp(-7P_\perp^2)$,[25] and we assumed that the lab momentum was unchanged in an elastic collision. For inelastic scattering the distribution of $P_\perp$ for both the primary and secondaries was taken as $\exp(-6P_\perp)$. The longitudinal momentum distribution of the primary was assumed to be flat in the laboratory frame, while the secondaries were assumed to go as $\exp(-6.7X^2)$. Since very few collision products were accepted by the spectrometer, the correction factors were not very sensitive to these approximations.[34]

Using these distributions, we obtained the rejection efficiencies for S_1, S_3, and S_4 plotted in Fig. 28 for several momenta. Except for S_4, the rejection efficiencies were nearly 90% and were rather independent of momentum. The rejection efficiency of S_4 was momentum-dependent because there was no momentum analysis after S_4 and the products of higher momentum collisions were more sharply peaked, and thus more easily accepted by S_5.

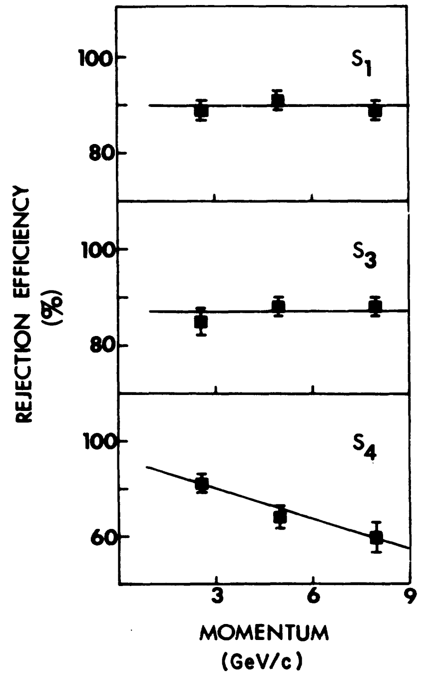

FIG. 28. The probability of losing an event after having a nuclear collision in S_1, S_3, and S_4 is plotted against the incident pion momentum.

Since any kaon or proton interacting in or before C_2 gave the wrong Čerenkov trigger, these particles had higher rejection efficiencies than pions. The estimated rejection efficiencies for p's and K's was 95% for all counters before S_2, and the same as for pions after S_2. Finally, note that a factor of 2 error in the number of in-scattered particles introduced only about a 3% error in the final correction factors.

To calculate the absorption in the steel vacuum chamber[35] we assumed an initial distribution of particles, allowed them to scatter in the chamber, and then determined the final distribution of their scattered products. The ratio of the final distribution to the initial distribution gave the effective rejections efficiency of the vacuum chamber for nuclear scattering $E_v(P, \theta)$. The correction factor was the product of this efficiency and the fraction of particles which interacted in the chamber.

We used Eq. (B4) for the initial distribution of particles leaving the diamond, and we used the scattering distributions described just above. We determined the final momentum P_f and horizontal angle θ_f of the emerging particles after each scattering. We also determined the probability χ that the scattered particle was within the vertical acceptance of the spectrometer. The horizontal trajectory of each particle was determined by projecting its actual trajectory onto the horizontal plane. The probability depended on the vertical scattering distribution and on the vertical acceptance of the spectrometer. The 5-cm vertical aperture of the septum magnet limited the in-scattering area of the vacuum chamber (dashed area in Fig. 29) to a few times the area normally accepted by the spectrometer, which is the shaded area in Fig. 29. Since this collimation limited the vertical acceptance to about $\frac{1}{3}$ of the mean-scattering angle, about $\frac{2}{3}$ of the scattered particles were lost.

More precisely at each point (P_f, θ_f) the final-particle distribution was the sum of the χ's, the probabilities for each event to give a particle which triggered the spectrometer. These χ's were calculated by the Monte Carlo program. This final distribution was essentially the integral

$$\frac{dN(P,\theta)^f}{d\Omega dP}=\iint\frac{dN(P_0,\theta_0)^i}{d\Omega_0 dP_0}\left[\frac{d\sigma(P_0;P,\theta_0-\theta)^{\text{inel}}}{d\Omega dP}+\delta(P-P_0)\frac{d\sigma(P_0;\theta_0-\theta)^{\text{el}}}{d\Omega}\right]d\Omega_0 dP_0, \tag{B5}$$

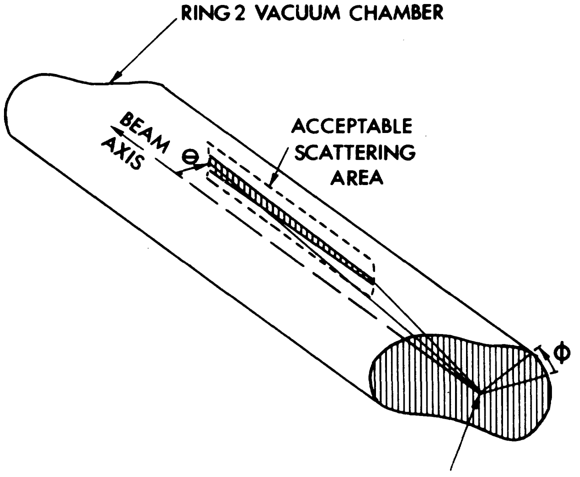

FIG. 29. Diagram showing the area of the vacuum chamber that can scatter a particle into our spectrometer (dashed) and the area traversed by unscattered particles, which are going into the spectrometer (shaded).

where P_0 and θ_0 are the momentum and horizontal angle of the incident particle. We compared this final distribution to the initial distribution to obtain the rejection efficiency of the vacuum chamber:

$$E_v(P,\theta)=\frac{[dN(P,\theta)/d\Omega dP]^i-[dN(P,\theta)/d\Omega dP]^f}{[dN(P,\theta)/d\Omega dP]^i}. \tag{B6}$$

The calculated rejection efficiencies for pions ranged from about 0.9 at 80 mrad to 0.5 at 200 mrad, and varied only slightly with momentum. For kaons and protons the efficiencies were somewhat greater because secondary pions did not give the proper Čerenkov trigger. These rejection efficiencies times the probability of interacting in the vacuum chamber gave the correction factors listed in Table IV.

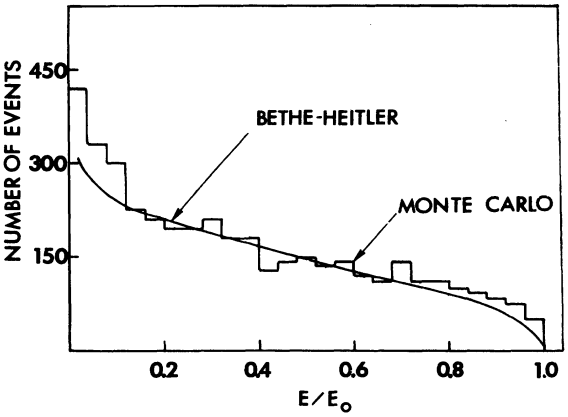

FIG. 30. Comparison of the positron energy-loss spectra calculated by the Monte Carlo program and by the Bethe-Heitler formula.

APPENDIX C: POSITRON CORRECTIONS

Finally we briefly describe the calculation of the positron contamination due to photons converting in the vacuum chamber. The photons came from decays of π^0's produced in beam-beam and beam-gas collisions. We assumed the π^0 spectrum was the same as the π^+ spectrum given in Eq. (B4). The π^0's were assumed to decay into photons isotropically in the π^0 center-of-mass system. The photon momenta were transformed into the laboratory frame and the photons were traced to the vacuum chamber. Here they were allowed to convert with a probability for pair production per radiation length of 0.78.[36] The produced positrons were assumed to have a flat energy distribution from 0 to the energy of the parent photon.[37] Each positron passed through the remainder of the vacuum chamber and the spectrometer, and could bremsstrahlung in this material. The energy spectrum of the bremsstrahlung radiation was chosen to fit

$$E'\varphi(E,E')=\text{constant}\quad(0\leq E'\leq E), \tag{C1}$$

where $\varphi(E,E')$ is the differential probability per radiation length for a positron of energy E to emit a photon of energy E'. This is in good agreement with more exact expressions[38] for $\varphi(E,E')$. The differential energy loss of the positron with distance dx was assumed to be

$$dE=E\frac{dx}{L_{\text{rad}}}, \tag{C2}$$

where E is the energy of the positron, and L_{rad} is the radiation length of the material. The average energy of the positrons thus had the proper exponential fall off with radiation length. The final energy spectrum of the positrons after bremsstrahlung also agreed adequately with the Bethe-Heitler formula[39] as shown in Fig. 30.

For both photon conversion and bremsstrahlung we assumed the final particle had the same angle as the original particle. The actual scattering angles were 1 mrad or less and were ignored.[40] Since the positrons had the same trajectory as the initial photons, the positron corrections were independent of the position of origin in the diamond.

[*] Work supported by a research grant from the U. S. Atomic Energy Commission.

[†] Royal Society European Exchange Fellow. Present Address: N. P. Division, CERN, 1211 Geneva 23, Switzerland.

[‡] Supported by Istituto Nazionale di Fisica Nucleare, Sezione di Bologna.

[§] Present Address: Department of Physics, University of California, La Jolla, California 92037.

[‖] John Simon Guggenheim Memorial Fellow.

[1] C. W. Akerlof, D. G. Crabb, J. L. Day, N. P. Johnson, P. Kalbaci, A. D. Krisch, M. T. Lin, M. L. Marshak, J. K. Randolph, P. Schmueser, A. L. Read, K. W. Edwards, J. G. Asbury, G. J. Marmer, and L. G. Ratner, Phys. Rev. D 3, 645 (1971); L. G. Ratner *et al.*, Phys. Rev. Lett. 18, 1218 (1967), and Phys. Rev. 166, 1353 (1968).

[2] J. V. Allaby, F. Binnon, A. N. Diddens, P. Duteil, A. Klovning, R. Meunier, J. P. Peigneux, E. J. Sacharidis, K. Schlüpmann, M. Spighel, J. P. Stroot, A. M. Thorndike, and A. M. Wetherell, CERN Report No. 70-12, 1970 (unpublished).

[3] E. W. Anderson, E. J. Blesser, G. B. Collins, T. Fujii, J. Menes, F. Turkot, T. A. Carrigan, R. M. Edelstein, N. C. Hien, T. J. McMahon, and I. Nadelhaft, Phys. Rev. Lett. 19, 198 (1967).

[4] R. P. Feynman, Phys. Rev. Lett. 23, 1415 (1969).

[5] J. Benecke, T. T. Chou, C. N. Yang, and E. Yen, Phys. Rev. 188, 2159 (1969); T. T. Chou and C. N. Yang, Phys. Rev. Lett. 25, 1072 (1970).

[6] D. W. Kerst, F. T. Cole, H. R. Crane, L. W. Jones, L. J. Laslett, T. Ohkawa, A. M. Sessler, K. R. Symon, K. M. Terwilliger, and N. Vogt-Nilsen, Phys. Rev. 102, 590 (1956).

[7] D. B. Lichtenberg, R. G. Newton, and M. H. Ross, MURA Report No. 100, 1956 (unpublished).

[8] G. K. O'Neill, Phys. Rev. 102, 1418 (1956).

[9] There has been interest shown in pion colliding beams; see R. Macek and B. Maglić, Part. Accel. 1, 121 (1970).

[10] W. C. Middelkoup and A. Schoch, CERN Report No. AR/Int SG/63-40, 1963 (unpublished).

[11] E. M. Rowe, J. W. Hicks, R. G. Johnson, G. M. Lee, H. R. Meier, and J. E. O'Mears, in Proceedings of the International Symposium on e^- and e^+ Storage Rings, Saclay, 1966, p. III-3-1 (unpublished).

[12] W. C. Barber, B. Gittelman, G. K. O'Neill, and B. Richter, Proceedings of the International Symposium on e^- and e^+ Storage Rings, Saclay, 1966, p. III-2-1 (unpublished).

[13] CERN Courier 8, No. 11 (1968).

[14] Disposal of beam of 10^{14} protons during a magnet or vacuum failure is a serious problem; such a beam could easily bore a hole through the vacuum chamber wall. This has actually occurred; see CERN Courier 12, No. 4, 127 (1972). To avoid this, there are beam dumps for each ring at the ISR. Each consists of a magnet which deflects the beam by a small vertical angle into a hole through a 2-m long stainless steel-titanium absorbing block. The magnet is interlocked with the essential ISR systems and in the event of a failure the magnet goes off and the beam is dumped within msec.

[15] We thank Muratori, Nichol, and the CERN Čerenkov group for supplying these counters.

[16] CPS User's Handbook Ref. 3 (unpublished).

[17] S. Penner, Rev. Sci. Instrum. 32, 150 (1961).

[18] We thank Professor F. Heymann, University College, London for suggesting these sources.

[19] The counters sometimes became radioactive and gave a large background in the spectrum, but as long as the peak was visible and did not move, the counter was known to be unchanged.

[20] K. Unser, CERN Report No. ISR-CO/69-6, 1969 (unpublished).

[21] C. Barbiellini *et al.*, CERN Report (unpublished).

[22] S. Van der Meer, CERN Report No. ISR-PO/68-31, 1968 (unpublished).

[23] Our normalization was in general agreement with the h_{eff} values found by other experimental groups working at other intersections; G. Cocconi *et al.*, C. Rubbia *et al.*, and J. C. Sens *et al.* (private communications).

[24] M. J. Longo and B. J. Moyer, Phys. Rev. 125, 701 (1962); A. Ashmore, G. Cocconi, A. N. Diddens, and A. M. Wetherell, Phys. Rev. Lett. 5, 576 (1960).

[25] LBL Particle Data Group, Review of Particle Properties, Phys. Lett. 39B, 1 (1972); A Compilation of K^+N Reactions, UCRL-20000 K^+N; A Compilation of π^+N Reactions, UCRL-20000 π^+N; A Compilation of NN Reactions, UCRL-20000 NN.

[26] We used $R_{pp} = 1$, $R_{\pi p} = 0.67$, and $R_{Kp} = 0.50$.

[27] M. C. Albrow, D. P. Barber, A. Bogaerts, B. Bosnjakovic, J. R. Brooks, A. B. Clegg, F. C. Erne, C. N. P. Gee, A. D. Kanaris, A. Lacourt, D. H. Locke, P. G. Murphy, A. Rudge, J. C. Sens, and F. Van der Veen, Phys. Lett. 40B, 136 (1972). This result and others seem to also support scaling at least in some X, $P_\perp$ region. But these groups are still taking data and have not yet published final results.

[28] Some of the accelerator data were interpolated by about 30% to the proper $P_\perp$ values using plots of the cross section against $P_\perp{}^2$. The pion accelerator data at $P_\perp{}^2 = 0.16$ shown in Ref. 29 were 15% low because of improper interpolation. An additional interpolation error of 5% was included in the present plot.

[29] L. G. Ratner, R. J. Ellis, G. Vannini, B. A. Babcock, A. D. Krisch, and J. B. Roberts, Phys. Rev. Lett. 27, 68 (1971); in *Particles and Fields—1971*, proceedings of the 1971 Rochester Meeting of the Division of Particles and Fields of the American Physical Society, edited by A. C. Melissinos and P. F. Slattery (A.I.P., New York, 1971).

[30] E. Yen and E. Berger, Phys. Rev. Lett. 24, 695 (1970).

[31] A. D. Krisch, Phys. Rev. 135, B1456 (1964); *Lectures in Theoretical Physics*, edited by W. E. Britten *et al.* (Univ. of Colorado Press, Boulder, 1966), Vol. 9, 1; and in *Proceedings of the Canadian Institute of Particle Physics Summer School, McGill University, 1972*, edited by R. Henzi and B. Margolis (McGill Univ. Press, Montreal, 1973), p. 233.

[32] K. Huang, Phys. Rev. 156, 1555 (1967).

[33] E. L. Berger, B. V. Oh, and G. A. Smith, Phys. Rev. Lett. 29, 679 (1972).

[34] We ignored the possibility that the scattered primary might have been a neutral (neutron or π^0). Since the rejection efficiencies were 85–95%, only 5–15% of the scattered particles were accepted; half of these were elastically scattered. Therefore if 50% of the inelastic primaries were neutral, we would lose only an addition-

al 1–4% of the scattered events. Since the maximum correction for nuclear absorption was 40%, ignoring neutrals amounted to, at most, a 2% error.

[35] The collision length for steel which we used was 9.6 cm. This was obtained from an unpublished experimental report by K. Stanfield, who calculated the total cross sections by means of an optical model, using a Woods-Saxon potential for the distribution of matter in the nucleus. These results were in reasonable agreement with the data for nuclei of high atomic number given in Ref. 24.

[36] B. Rossi, *High Energy Particles* (Prentice-Hall, Englewood Cliffs, New Jersey, 1952), p. 81, Eq. (13).

[37] Ref. 36, p. 82, Fig. 2.19.1.

[38] Ref. 36, p. 51, Fig. 2.11.2.

[39] H. A. Bethe, W. Heitler, Proc. R. Soc. Lond. A146, 63 (1934).

[40] See Ref. 36, p. 53, Eq. (19), and p. 83. Eq. (16).

PHYSICAL REVIEW D VOLUME 9, NUMBER 5 1 MARCH 1974

Production of f^0 mesons in 4.5-GeV/c $\pi^- p$ interactions*

L. E. Holloway, B. Huld,† M. Jordan,‡ U. Koetz,§ U. E. Kruse, D. W. Mortara,‖ and L. J. Nodulman
University of Illinois at Urbana, Illinois 61801

S. Bernstein, S. Margulies, and D. W. McLeod
University of Illinois at Chicago Circle, Chicago, Illinois 60680

(Received 23 July 1973)

An optical spark chamber and neutron time-of-flight spectrometer experiment studied the reaction $\pi^- p \to \pi^+\pi^- n$ at incident pion momentum of 4.5 GeV/c in the mass region of the f^0 meson. Analysis of the data shows no evidence for anomalous structure in the f^0 mass spectrum. The two-pion differential cross section in the f^0 region is consistent with Wolf's one-pion-exchange model for momentum transfers (squared) $-t \lesssim 0.7$ (GeV/c)^2. The differential cross section is larger than that predicted at high momentum transfer, and may be attributed to natural-parity-exchange contributions as evidenced in the f^0 decay distribution.

I. INTRODUCTION

There has been considerable controversy and conflicting experimental data on the existence of a split structure for the A_2 meson. Contradictory reports of possible structure in the f^0 mass spectrum have also been published.[1] The A_2 and f^0 mesons belong to the same ($J^P = 2^+$) SU(3) nonet, and may be expected to exhibit similar characteristics.

Production of f^0 mesons has been reasonably well studied at low momentum transfer[2]; however, the data have been statistically limited for momentum transfers squared beyond $|t| \sim 0.6$ (GeV/c)^2. The decay angular distribution is fairly well characterized by one-pion-exchange (OPE) production with some interference from an s-wave dipion state. The differential cross section $d\sigma/dt$ for f^0 production has been well described by OPE with absorption, or by Wolf's one-pion-exchange model.[3]

We report here results of a neutron-counter time-of-flight/optical spark chamber experiment studying the reaction $\pi^- p \to \pi^+\pi^- n$ at 4.5 GeV/c incident π^- momentum. Features of the spectrometer include high missing-mass resolution and uniform acceptance for f^0 production over a broad range of momentum transfer, $0.125 < |t| < 1.6$ (GeV/c)^2.

We find no evidence for splitting of the f^0 mass spectrum. We also find that f^0 production at high momentum transfer [$|t| > 0.7$ (GeV/c)^2] is more copious than expected from an OPE model and is characterized by natural parity exchange.

II. EXPERIMENTAL DETAILS

The experiment was performed in the 17° beam of the Argonne ZGS. Figure 1 shows the apparatus surrounding the 30-cm liquid hydrogen target. A larger view showing the neutron flight path is provided in Fig. 2. The apparatus was similar to that of a previous experiment studying the ω meson.[4] However, in order to improve mass resolution several changes were made. The essential differences were as follows:

1. A fifteen-element scintillation hodoscope (M) was placed at the first (momentum dispersed) focus of the beam.

2. The horizontal displacement and angle of the incident pion was measured by two multiwire proportional counters (MWPC) placed one meter apart in front of the hydrogen target. Each consisted of 20 wires spaced 2 mm apart.[5] The momentum hodoscope and MWPC information determined the